Micromechanical investigation of the asymptotic behaviour of granular materials

Bo Liu [a], Zhen-Yu Yin [a,*], Pierre-Yves Hicher [b]

[a] *Department of Civil and Environmental Engineering, The Hong Kong Polytechnic University, Hung Hom, Kowloon, Hong Kong, China*
[b] *Research Institute in Civil and Mechanical Engineering (GeM), UMR CNRS 6183, Ecole Centrale de Nantes, Nantes, France*

ARTICLE INFO

ABSTRACT

Laboratory experiments have shown that the proportional shearing of granular materials along arbitrary strain path directions will lead to stress states that converge asymptotically to proportional stress paths with constant stress ratios. The macro- and microscopic characteristics of this asymptotic behaviour, as well as the existence of asymptotic states exhibiting a constant stress ratio and a steady strain-rate direction, have been studied using the discrete element method (DEM). Proportional shearing along a wide range of strain-rate directions and from various initial stress/density states has been conducted. The simulation results suggest that general contractive asymptotic states (except for isotropic states) do exist but may be practically unattainable. Dilative strain path simulations, on the other hand, result in continuously changing stress ratios until static liquefaction occurs, indicating the absence of dilative asymptotic states. Despite this difference, a unique relationship between the stress increments and the current stress ratio gradually emerges from all strain path simulations, regardless of strain path direction and initial stress/density conditions. At the particle scale, the granular assembly sheared along proportional strain paths exhibits a constant partition ratio between strong and weak contacts. Although general proportional strain paths are associated with changing geometric and mechanical anisotropies, the rates of change in these anisotropies for contractive strain paths are synchronised to maintain a constant ratio of their contributions to the mobilised shear strength of the material, with a higher proportion being contributed by geometric anisotropy for more dilative strain paths.

1. Introduction

Granular materials have been found to attain unique proportional stress states after undergoing sufficient shearing along some specific loading paths. Notable examples of these paths include the constant-volume (undrained) shearing, oedometer and isotropic compression paths. After an initial complex response, these paths ultimately lead to critical state (CS), K_0 state and isotropic stress state, respectively, all characterised by constant ratios between the effective principal stresses. Inspired by these observations, the geotechnical community has put forth a conjecture that granular materials subjected to sustained shearing along any arbitrary proportional strain path will ultimately attain a unique proportional stress state (Gudehus et al., 1977; Ibraim et al., 2010; Lensky, 1960). This behaviour was called 'asymptotic behaviour' by Gudehus et al. (1977) and was characterised in a formal manner by Goldscheider (1976) through two governing rules:

Rule 1: Proportional strain paths starting from a stress-free state ($p'=q=0$) are associated with proportional stress paths.
Rule 2: Proportional strain paths starting from an arbitrary stress state lead to stress paths that asymptotically converge to the corresponding proportional stress path reached by the initially stress-free sample.

Laboratory strain path testing has been used to study the asymptotic behaviour of soils, with a greater number of studies focusing on sand as compared to clay (Topolnicki et al., 1990). These experiments covered a wide variety of testing conditions, including axisymmetric triaxial tests (Darve et al., 2007; Lancelot et al., 2004), plane-strain compression (Wanatowski, 2007; Wanatowski et al., 2008), biaxial shear with rotation of principal axes (Ibraim et al., 2010), and true triaxial tests (Chu and Lo, 1994). The experiments have invariably pointed out a tendency of sand to approach asymptotic states and showed that both the initial and asymptotic behaviours depended on the imposed strain path

direction. As the strain path shifts from contractive to more dilative, the asymptotic stress ratio increases until the imposed dilatancy exceeds the peak dilatancy exhibited by a sample of the same relative density in a drained test (Chu and Lo, 1994; Ibraim et al., 2010; Wanatowski et al., 2008). In such cases, the asymptotic stress ratio is bounded by the failure stress ratio. Besides, it has been shown that a mildly contractive strain path imposed on a loose granular material can lead to an initial decrease in the mean stress before reaching the asymptotic state with steadily increasing stresses (Darve et al., 2007; Lancelot et al., 2004).

One major limitation of existing experimental studies is that a fairly constant stress ratio has rarely been attained before reaching high strain levels where non-homogeneous deformations, such as shear bands, may develop (Chu et al., 1996). As a result, laboratory element tests can only provide reliable element responses up to a certain strain level where a well-defined asymptotic state may not have been reached, especially for samples subjected to dilative strain paths (Wanatowski, 2007). Furthermore, in axisymmetric, plane-strain and true triaxial tests, the strain path direction is typically indicated with $d\varepsilon_v/d\varepsilon_a$ ($d\varepsilon_v$ and $d\varepsilon_a$ are the increments of volumetric strain ε_v and axial strain ε_a over the same time increment, respectively). The range of $d\varepsilon_v/d\varepsilon_a$ achieved in existing experiments is limited between -1.4 and 1.0 due to difficulties associated with precise strain control and the limited capacity of the stress measurement device.

The deficiencies identified above highlight the need to examine the attainability of asymptotic states across a wider range of strain path directions while preventing stress and deformation inhomogeneities. The difficulty associated with strain control and measuring capacity can be easily circumvented by simulating proportional shearing tests using DEM. In the literature, several DEM simulations have been reported that studied the response of granular materials to proportional shearing. However, strain path testing was used in several studies simply as a technique to apply partially drained conditions (Darve et al., 2007; Nicot et al., 2013) with no emphasis on the asymptotic behaviour. Besides, many existing DEM studies employed rigid wall boundaries (Deng et al., 2021; Shi and Guo, 2017; Wu et al., 2024), leading to shear band formation for dilative strain paths ($d\varepsilon_v/d\varepsilon_a < 0$). In fact, the stress and deformation inhomogeneities due to shear banding can be suppressed by applying periodic boundary conditions (Cundall, 1988; O'Sullivan, 2011; Thornton, 2000). Mašín (2012) studied the asymptotic behaviour using DEM simulations along a wide spectrum of constant strain-rate directions with $d\varepsilon_v/d\varepsilon_a$ ranging from -1.0 to 3 by employing the periodic boundary condition. However, this study focused exclusively on macroscopic behaviours without exploring the associated micro mechanisms. Zhou et al. (2016) investigated the material fabric variations along proportional paths using a DEM model that accounted for rolling resistance between particles. However, this study primarily focused on the effect of rolling resistance rather than the influence of strain path direction on fabric evolution. In addition, none of these existing studies have explicitly demonstrated that a constant stress ratio can be ultimately attained for general proportional strain paths (i.e. $d\varepsilon_v/d\varepsilon_a \neq 0$ and 3).

Although general asymptotic states are inherently embedded in many constitutive theories, including CS-based models and hypoplasticity (Bauer et al., 2020; Kolymbas, 2012; Mašín, 2012), many studies (Kolymbas, 2012; Luo et al., 2009; Mašín, 2013; Medicus et al., 2016) showed that explicitly incorporating asymptotic behaviour into constitutive theories can simplify formulations and enhance predictive capabilities. Among these efforts, Kolymbas (2012) and Medicus et al. (2016) developed hypoplastic models relying on backbone $R - D$ relationships, i.e. the relationship between the direction of stress (R) and the direction of straining (D), that quantitatively satisfy only a limited number of specific asymptotic states. In comparison, Luo et al. (2009) integrated a special $R - D$ relationship, i.e. the empirical $q/p' - d\varepsilon_v/d\varepsilon_a$ relationship experimentally observed by Chu and Lo (1994), into an elastoplastic model, where q is the deviatoric stress and p' is the mean effective stress. These studies emphasise the need for a more general and

realistic $R - D$ relationship to facilitate quantitative comparisons with experimental data. An improved understanding of asymptotic behaviour and the underlying micromechanics is essential for developing this relationship.

This study aims to examine the practical attainability of general asymptotic states and identify microstructural characteristics that are most representative of the asymptotic behaviour using DEM simulations. Here, the asymptotic behaviour is understood as the granular material response during the course of approaching the asymptotic states, meaning that such behaviour can exist even if general asymptotic states are practically unattainable. The simulation parameters were selected to mitigate the rate effects and nonnegligible interparticle overlap identified in previous studies (Mašín, 2012; Mašín and Jerman, 2015) so that physically sound and quasi-static processes of proportional shearing can be approached.

2. DEM simulations

2.1. DEM model details

The DEM simulations were performed using the commercial software PFC3D 6.0 on an assembly of 56,419 spherical particles within a $10 \times 10 \times 10$ mm^3 cubic domain, as shown in Fig. 1. Periodic boundaries were used to ensure that an external strain field could be uniformly applied across the whole domain. With this boundary condition, particles leaving through one boundary would re-enter from the opposite side with the same speed, as if the model was surrounded along all edges by identical granular packings. As discussed earlier, the periodic boundary is capable of reducing the boundary effects and suppressing the occurrence of strain localisation (Cundall, 1988; O'Sullivan, 2011; Thornton and Antony, 2000) since it imposes kinematic constraints that ensure continuity of deformations across opposing boundaries. As a result, shear bands are kinematically permissible only at specific angles that are mechanically inadmissible in general.

The particles were generated randomly in a nonoverlapping state following the particle size distribution presented in Fig. 2. This distribution is a modification of the Rosin-Rammler distribution, which has been widely used to describe the particle size distribution of granular
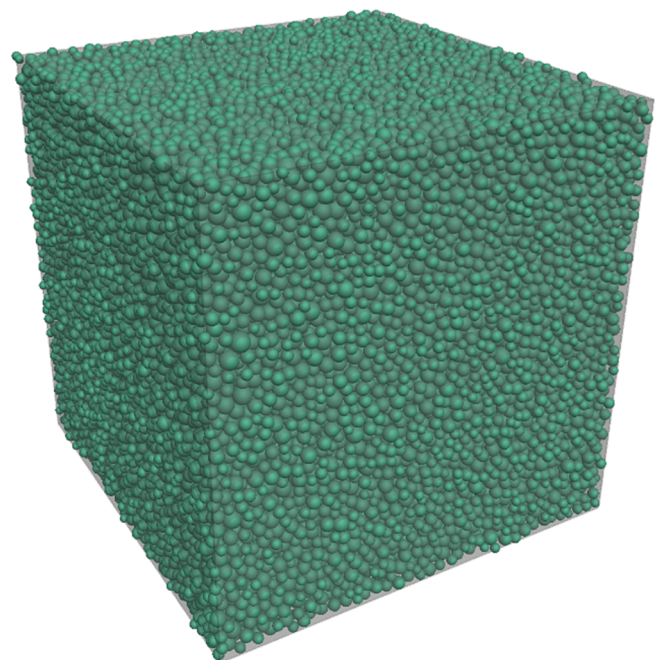

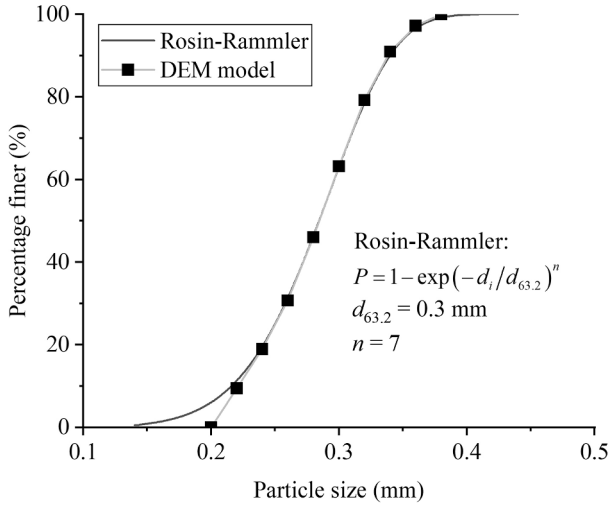**Fig. 1.** DEM model of a polydisperse granular assembly with 56,419 spherical particles.

Fig. 2. Particle size distribution of the DEM assembly.

materials (Kumar et al., 2020; Perfect et al., 1998). The characteristic sizes d_0, d_{50} and d_{100} of this gradation are 0.2, 0.29 and 0.38, respectively, where the subscript denotes the mass percentage of particles finer than the corresponding size. The non-overlapping state is considered the stress-free state from which the proportional stress path is expected to be attained following a prescribed proportional strain path. To facilitate comparison between the responses in different simulations, all subsequent DEM simulations were performed on different *clones* of this nonoverlapping sample. Thus, results from different simulations represent the behaviour of the same sample subjected to different loading paths.

The particle–particle interaction was simulated using the Hertz contact model provided in the software package, which simulates a contact response similar to that predicted by Mindlin and Deresiewicz's theory (1953). The contact normal force (f_n) in a Hertzian contact between two spheres with radii R_1 and R_2 is calculated as follows:

$$f_n = \frac{4G_p}{3(1-\nu_p)}\sqrt{\frac{R_1 R_2}{R_1+R_2}}\delta_n^\alpha \tag{1}$$

where G_p and ν_p are the shear modulus and Poisson's ratio of the particles, δ_n is the interparticle overlap, and α is a constant that takes a value of 1.5 according to Mindlin and Deresiewicz's theory.

The contact shear force is calculated incrementally following Eq. (2), where f_s^0 is the contact shear force at the beginning of the timestep, $\Delta\delta_s$ is the increment of relative shear displacement occurring during the current timestep, and k_s is the contact shear stiffness which depends on the current contact normal force according to Eq. (3).

$$f_s = f_s^0 - k_s \cdot \Delta\delta_s \tag{2}$$

$$k_s = \frac{8G_p}{3(2-\nu_p)}\sqrt{\frac{R_1 R_2}{R_1+R_2}}|F_n|^{(\alpha-1)/\alpha} \tag{3}$$

In the Hertz contact model, the magnitude of the contact shear force is regulated by a maximum value given by $\mu|f_n|$ where μ is the coefficient of friction. In this study, G_p and ν_p took the typical values of 29 GPa and 0.22, respectively, according to the measurements made on glass and quartz by Grabco et al. (2002) and Cavarretta (2009). The friction coefficient, μ, which varies with the surface roughness, was given a typical value of 0.4, considering that using $\mu \geq 0.5$ is shown by Huang et al. (2014) to result in unrealistic critical state behaviour.

2.2. Simulation program and procedures

To study the influence of initial conditions, the DEM sample was subjected to different proportional strain paths from different initial states. For simplicity, only axisymmetric strain paths were considered, and the major principal strain rate was always compressive (i.e. $d\varepsilon_a > 0$). Therefore, the accessible values of $d\varepsilon_v/d\varepsilon_a$ range from negative infinity to 3, with $d\varepsilon_v/d\varepsilon_a > 0$ standing for compressive strain paths and $d\varepsilon_v/d\varepsilon_a < 0$ representing dilative strain paths. Specifically, $d\varepsilon_v/d\varepsilon_a = 0$, 1 and 3 correspond to constant-volume (undrained) shearing, 1D compression and isotropic compression, respectively. According to the DEM study by Mašín (2012), the minimum $d\varepsilon_v/d\varepsilon_a$ that can be practically attained in strain path testing is about −1, as lower values of $d\varepsilon_v/d\varepsilon_a$ will be associated with very low stress levels (<0.5 kPa) and hence significantly scattered responses. Therefore, the range of $d\varepsilon_v/d\varepsilon_a$ considered in this study is −1 to 3.

The initial condition from which a proportional strain path is initiated determines the length of shearing required for the asymptotic state to be attained or whether the asymptotic state can be obtained or not. Compressive strain paths ($d\varepsilon_v/d\varepsilon_a > 0$) can be imposed from arbitrary initial conditions whereas dilative strain paths ($d\varepsilon_v/d\varepsilon_a < 0$) starting from a stress-free sample cannot be considered. Therefore, four groups of proportional strain path simulations have been defined, as summarised in Table 1. Starting from a stress-free state, the simulations in Group A are expected to reach the asymptotic state, thus providing benchmarks for examining the responses obtained from Group B where the proportional strain path loading was imposed following an isotropic compression to $\sigma_1' = \sigma_2' = \sigma_3' = 10$ kPa from the stress-free state. Note that the interparticle friction used in the isotropic compression (μ_{prep}) takes the same value as the one in proportional strain path testing, producing a sample behaving like a loose sand.

The simulations in Group C consisted of proportional shearing tests along dilative and constant-volume strain paths. These simulations were initiated from an isotropic state with a high stress level of 10 MPa in order to achieve sufficient deformation before the stresses drop to negligible values, in the hope that the asymptotic state could be reached at stress levels high enough for the responses to be more reliable. In Group D, three additional strain path simulations were conducted for $d\varepsilon_v/d\varepsilon_a = -0.5$ on samples of different initial void ratios under the same initial stress state as in Group C. In the sample preparation process (isotropic compression from the stress-free state), the frictional coefficient used was 0.1, 0.2 or 0.3, producing samples with initial void ratios of 0.603, 0.64 and 0.648, respectively. Group D was designed to investigate the effect of sample density on the response to proportional strain path shearing.

To guarantee that the test conditions were quasi-static, the loading rate was determined to ensure that the associated inertial number (I) was below 0.001 (Cerfontaine et al., 2021; Mašín and Jerman, 2015). The inertial number (I) is defined as (Da Cruz et al., 2005; Jop et al., 2006):

$$I = |\dot{\gamma}_s| d\sqrt{\frac{G_s}{p'}} \tag{4}$$

Table 1
Summary of the proportional strain path simulations.

Group	Initial condition	$d\varepsilon_v/d\varepsilon_a$ of the tested path/s
A	Nonoverlapping state; $e = 1.555$	1.0 / 1.5 / 2.0 / 2.5 / 3.0
B	$\sigma_1 = \sigma_2 = \sigma_3 = 10$ kPa; $\mu_{prep} = 0.4$; $e = 0.699$	0.5 / 1.0 / 1.5 / 2.0 / 2.5
C	$\sigma_1 = \sigma_2 = \sigma_3 = 10$ MPa; $\mu_{prep} = 0.4$; $e = 0.664$	−1.0 / −0.75 / −0.5 / −0.25 / 0
D	$\sigma_1 = \sigma_2 = \sigma_3 = 10$ MPa; $\mu_{prep} = 0.1, 0.2, 0.3$; $e = 0.603, 0.640, 0.648$	−0.5

where $\left|\dot{\gamma}_s\right| = \sqrt{2\dot{\varepsilon}_{ij}\dot{\varepsilon}_{ij}}$ with $\dot{\varepsilon}_{ij}$ being the stretching rate tensor, d is a characteristic particle size, and p' is the mean effective stress.

According to Eq. (4), I is not a constant in a deformation process involving a changing mean stress. Fig. 3 shows the relationship between I and p' for $\left|\dot{\gamma}_s\right| = 2\,\text{s}^{-1}$ and d taking different characteristic particle sizes. The figure suggests that employing a stretching rate with $\left|\dot{\gamma}_s\right| = 2\text{s}^{-1}$ is able to maintain the condition of quasi-static loading for mean stresses as low as about 1 kPa. Consequently, the deformation rates imposed in all proportional strain simulations presented in this study were selected to satisfy $\left|\dot{\gamma}_s\right| = 2\text{s}^{-1}$.

Depending on the different strain paths followed, the final state reached in the simulations would involve either a monotonically increasing or decreasing stress level, except for the special case of un-drained shearing ($d\varepsilon_v/d\varepsilon_a = 0$) which leads to either liquefaction or critical state, see e.g. Guo and Zhao (2013), Nguyen et al. (2018). The simulations leading to the vanishing of stresses were terminated when the mean stress, p', decreased to 10 kPa, while the simulations with continuously increasing stresses were terminated once p' reached 10 MPa. As shown in Fig. 4, at p'=10 MPa, most interparticle contacts exhibit a relative overlap ratio, calculated as $\delta_n/(R_1 + R_2)$, smaller than 1 %, which is about the threshold below which the interparticle overlap can be considered negligible (Alonso-Marroquín et al., 2005).

3. Macroscopic responses and analysis

3.1. Contractive strain paths

Fig. 5(a) presents the stress path response in the $q – p'$ plane obtained from simulations conducted along contractive proportional strain paths ($d\varepsilon_v/d\varepsilon_a > 0$) from the initial state with $p'_0 = 10$ kPa (Group B). It can be seen from Fig. 5(a) that the stress path exhibits a nonlinear response at the beginning of the loading, followed by an almost linear increase. The initial nonlinear responses are better visualized in Fig. 5(b) where the stress paths are plotted on a double-logarithmic scale. Specifically, the simulation with $d\varepsilon_v/d\varepsilon_a = 0.5$ experienced an initial decrease in p' before a steady increase of p' and q. Such an initial decrease in p' is typically observed in loose sand subjected to slightly contractive strain paths (Darve et al., 2007; Hicher, 1998; Lancelot et al., 2004). Besides, as the strain path becomes less contractive (i.e. $d\varepsilon_v/d\varepsilon_a$ decreases), the slope of
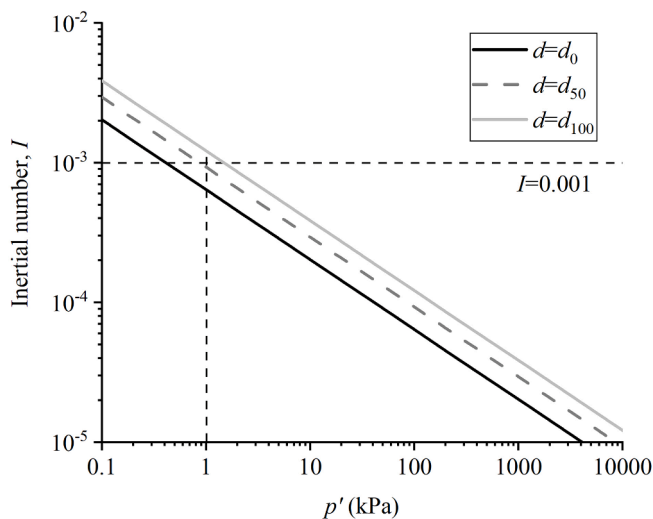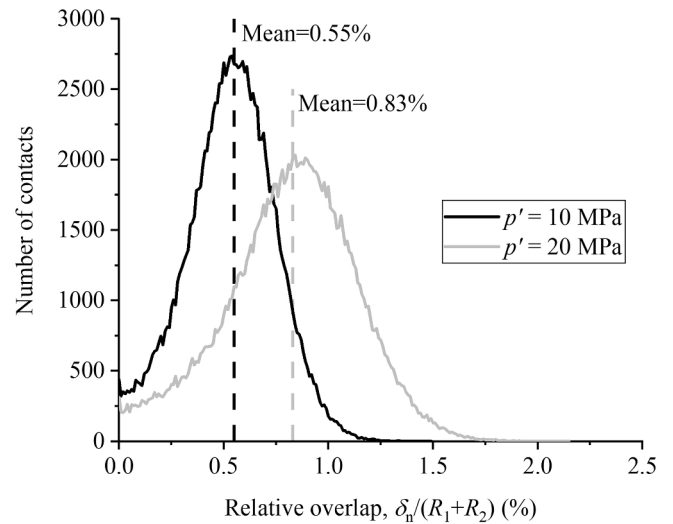

Fig. 4. The distribution of relative overlap at $p' = 10$ and 20 MPa for the isotropic compression simulation ($d\varepsilon_v/d\varepsilon_a = 3$).

the stress paths increases, indicating an increasing level of strength mobilisation, in agreement with previous observations (Chu et al., 1993; Daouadji et al., 2017; Wanatowski et al., 2008).

Fig. 6(a) shows that the stress ratios for the same sample subjected to different contractive strain paths all increase with a decreasing rate to approach an asymptotic value. The behaviour confirms Goldscheider's Rule 2. However, the corresponding simulations conducted on stress-free samples (Group A) do not yield a well-defined asymptotic stress ratio, as shown in Fig. 6(b). Instead, the stress ratios also continue to increase with further stretching as for Group B. One possible reason is that the level of strains applied in the simulations is insufficient, since the shearing was terminated once the mean stress reached 10 MPa.

To verify this hypothesis, an additional shearing up to a shear strain of 26.6 % was simulated in the case of $d\varepsilon_v/d\varepsilon_a = 0.5$ and $p'_0 = 10$ kPa, and the results are shown in Fig. 7. Also shown in the figure is the co-ordination number (CN) that quantifies the average number of contacts per particle (to be discussed in detail in Section 4.1). As expected, the stress ratio is seen to finally stabilise at $q/p' =0.88$, indicating that an asymptotic state has been reached. However, this was achieved after p' exceeds 90 MPa, well above the stress level required to trigger large-scale particle breakage in most sands (Hardin, 1985; Lade et al., 1996). Moreover, the asymptotic stress ratio of 0.88 is greater than the CS stress ratio of $M = 0.78$ determined using conventional drained triaxial shear simulations with $\sigma'_3 = 50$, 100 and 200 kPa. This unusual behaviour occurs because the interparticle overlaps are excessive at very high stress levels, leading to an unrealistic increase of CN that violates the geometric restrictions in real granular packings. The unrealistically high CN value spuriously increases the angularity of the particles and hence the strength of the material; Fei and Narsilio (2020), Cho et al. (2006), Santamarina and Cho (2004), among others, showed the tendency of CN and shear strength to increase as particles become more angular. Because of this, the simulated responses at very high stress levels (> 10 MPa) must be interpreted with caution, and additional shearing to very large strains has not been conducted for other contractive strain paths.

Despite the large-strain response in Fig. 7 being questionable, it seems reasonable to speculate that general asymptotic states for arbitrary contractive strain paths do exist but may be practically unattainable as they are associated with excessive stresses and hence particle breakage.
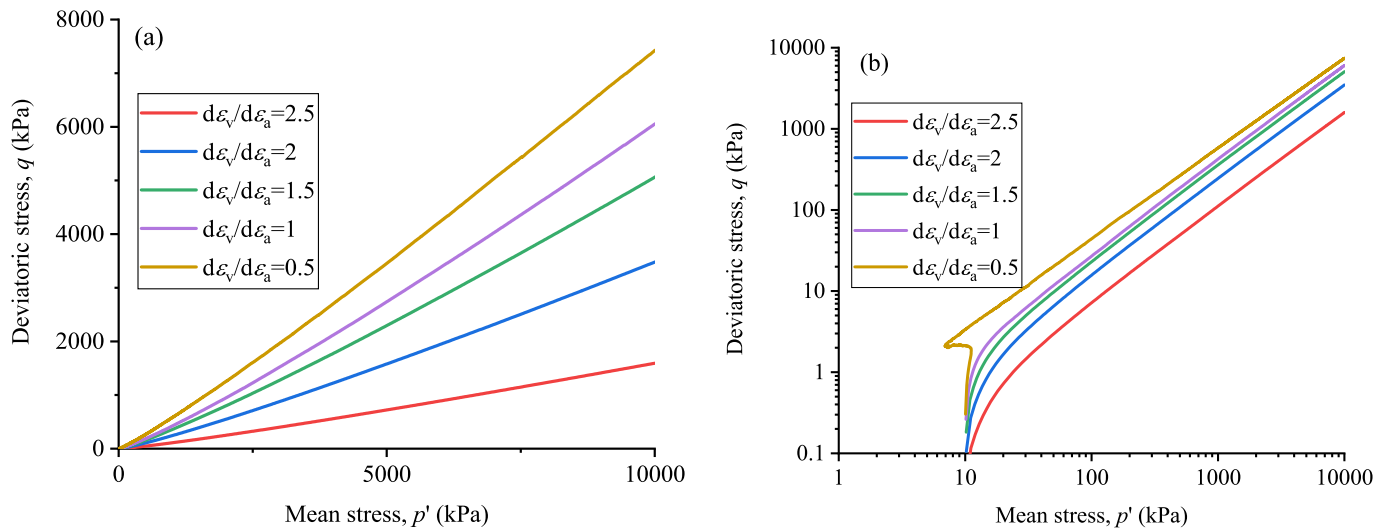

Fig. 3. Relationship between inertial number and mean stress for $\left|\dot{\gamma}_s\right| = 2\text{s}^{-1}$

Fig. 5. Stress path responses obtained from DEM simulations along contractive strain paths from an initial state with $p'_0 = 10$ kPa, plotted on a) arithmetic scale and b) double-logarithmic scale.
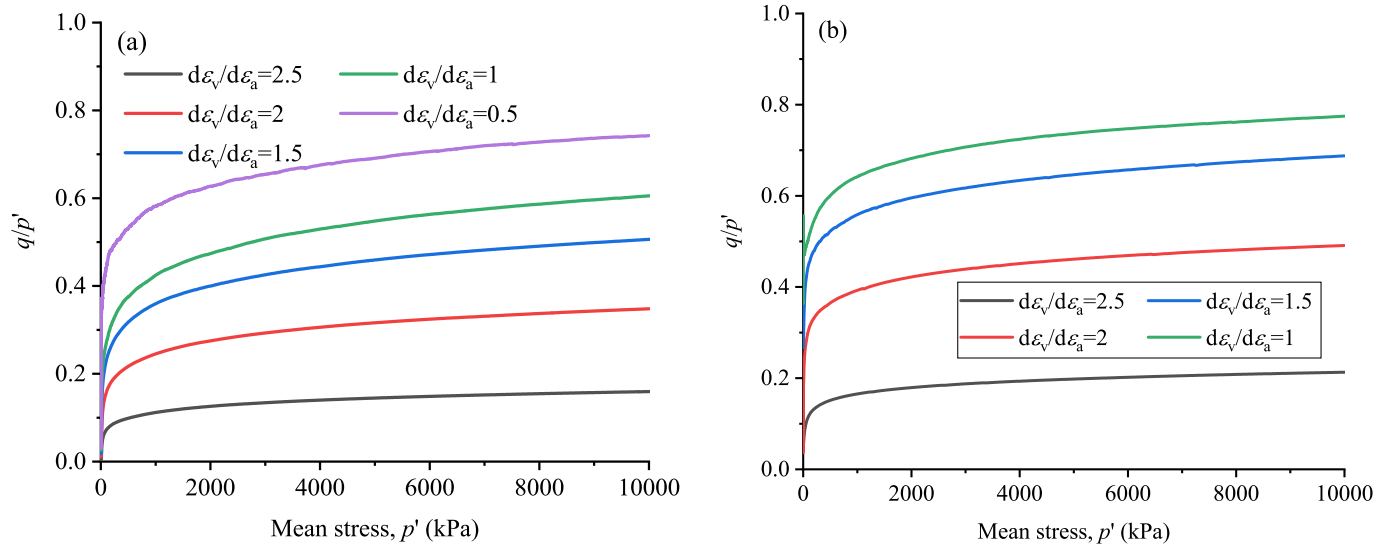

Fig. 6. Stress ratio response from simulations stretching along contractive proportional strain paths from a) an isotropic state with $p'_0 = 10$ kPa and b) the stress-free state.

3.2. Dilative strain paths

The stress path responses for Group C simulations are presented in Fig. 8. The stress paths show some differences during the initial stage of stretching, with a higher peak deviatoric stress reached for a less negative value of $d\varepsilon_v/d\varepsilon_a$. After the peak, the deviatoric stress starts to decrease, and the stress paths for negative values of $d\varepsilon_v/d\varepsilon_a$ almost converge to a single straight line passing through the origin. All the simulations with $d\varepsilon_v/d\varepsilon_a < 0$ finally reached a liquefied state with $p'=q = 0$. In contrast, the undrained shearing ($d\varepsilon_v/d\varepsilon_a = 0$) exhibited a different response, with a phase transformation occurring as the stress path approached the CSL. Following this transformation, the stress path ascended nearly along the CSL. This simulation was halted after a shear strain of 43 %. The above behaviours are generally in line with those observed in existing laboratory experiments for loose sand (Lancelot et al., 2004; Nicot et al., 2013; Wanatowski et al., 2008) and DEM simulations (Deng et al., 2021; Sibille et al., 2015). In the following analysis, attention will be paid to the cases with $d\varepsilon_v/d\varepsilon_a < 0$ as undrained shearing has been extensively studied in the literature.

The simulation results for samples of different initial densities (e_0) sheared along the same strain path direction of $d\varepsilon_v/d\varepsilon_a = -0.5$ are presented in Fig. 9. It is observed that the resulting stress paths all attained a seemingly linear trend after reaching the peak deviatoric stress that increases with the decrease of e_0. However, as shown in Fig. 9(b), the stress ratio does not remain constant after reaching the peak but decreases as shearing proceeds. Specifically, the peak stress ratio reached for the sample with $e_0 = 0.603$ surpasses the critical state line M at first and then drops below it as the stress state approaches the origin (static liquefaction).

From Fig. 9(b) and Fig. 8(b), it can be observed that there is no asymptotic state for negative values of $d\varepsilon_v/d\varepsilon_a$ irrespective of initial sample density or strain path direction. This observation is different from the findings of existing laboratory tests (Chu and Lo, 1994; Jrad et al., 2012; Wanatowski et al., 2008) and DEM simulations (Darve et al., 2007; Deng et al., 2021) where an asymptotic stress ratio was observed and appeared to be unaffected by the strain path direction. The current simulations differ from the existing studies in that the periodic boundaries were employed to suppress the development of shear bands, as
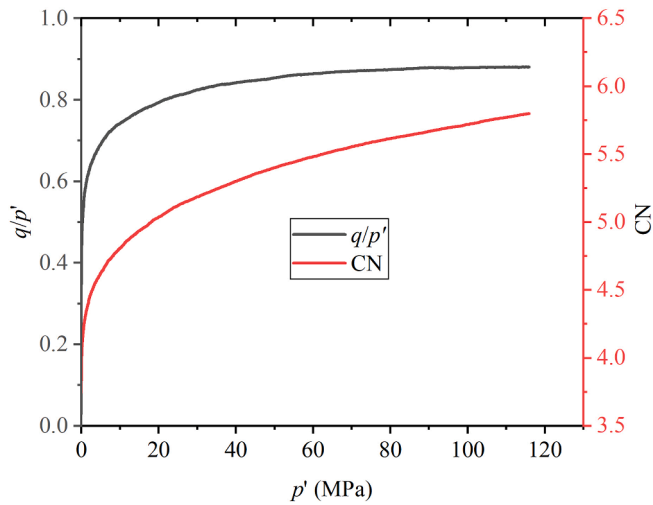
Fig. 7. Variation of stress ratio (q/p') and coordination number (CN) during prolonged shearing up to a shear strain of 26.6 % in the simulation with $d\varepsilon_v/d\varepsilon_a = 0.5$ and $p'_0 = 10$ kPa

discussed earlier. Fig. 10 presents the stress ratio response from a set of dilative strain path simulations where all simulation parameters were the same as those from Group C simulations except that rigid wall boundaries were employed. Fig. 10 clearly shows that constant stress ratios were almost obtained in these simulations, indicating that the asymptotic stress ratios for dilative proportional strain paths observed in existing laboratory tests and DEM studies are likely to be the result of deformation inhomogeneity within the samples (Deng et al., 2021).

3.3. A common characteristic for all proportional strain paths

The above results suggest that Goldscheider's two rules are generally satisfied for contractive strain paths although general asymptotic states may be practically unattainable. However, the stress ratios obtained from dilative strain path simulations do not exhibit any tendency to approach a constant value. It appears that the stress response along dilative proportional strain paths should be described differently from those along contractive proportional strain paths. However, upon a close examination of the data, it has been discovered that both contractive and dilative strain paths can be associated with the same incremental stress

response.

Axisymmetric stress states can be simply characterised by q and p', and the associated stress increment direction by dq/dp'. Fig. 11 presents the relationship between dq/dp' and q/p' derived from all the simulations listed in Table 1. In Fig. 11(a), the response from the simulation with $d\varepsilon_v/d\varepsilon_a = 0.5$ is omitted since the general trend is the same but the large scattering renders data interpretation difficult. From the figures, it is observed that following an initial nonlinear response, the $dq/dp' - q/p'$ curves for various $d\varepsilon_v/d\varepsilon_a$ values and different initial conditions all converge to a straight line that can be represented by:

$$\frac{dq}{dp'} = \alpha \frac{q}{p'} \tag{5}$$

where α is the slope of the line, which is found to be about 1.09 for simulations conducted from the stress-free state and 1.15 for the other simulations. Neglecting the small difference between the values of α derived from all these simulations, the behaviour presented in Fig. 11 suggests that the tendency to converge to a unique $dq/dp' - q/p'$ relationship is a common characteristic of all proportional strain path simulations, irrespective of initial conditions and strain path directions.

Through rearranging and integrating Eq. (5), Eq. (6) can be obtained:

$$\frac{q}{p'} = A \left(\frac{p'}{P_a} \right)^{\alpha - 1} \tag{6}$$

where A is a constant depending on the material type and strain path direction $d\varepsilon_v/d\varepsilon_a$; P_a is the atmospheric pressure (~101 kPa) used for normalisation.

From Eq. (6), it appears that for the stress ratio to attain a constant value after sufficient shearing, α cannot be a constant, but instead must decrease to 1 as shearing continues. In fact, in the simulation with prolonged shearing along $d\varepsilon_v/d\varepsilon_a = 0.5$ path, a clear decrease of α towards 1 can be observed, as shown in Fig. 12 where the value of α was calculated as the ratio of dq/dp' to q/p' according to Eq. (5). In summary, during proportional shearing, an almost proportional $dq/dp' - q/p'$ relationship described by Eq. (5) appears first. Accompanied by α decreasing to 1, this relationship recovers Goldscheider's two rules.

The above analysis can explain why the value of α determined from the simulations on the stress-free sample is smaller: the value of α-1 measures the distance between the current state and the anticipated asymptotic state. Loading from the stress-free state can approach the asymptotic state faster as it is easier to modify the fabric of a stress-free
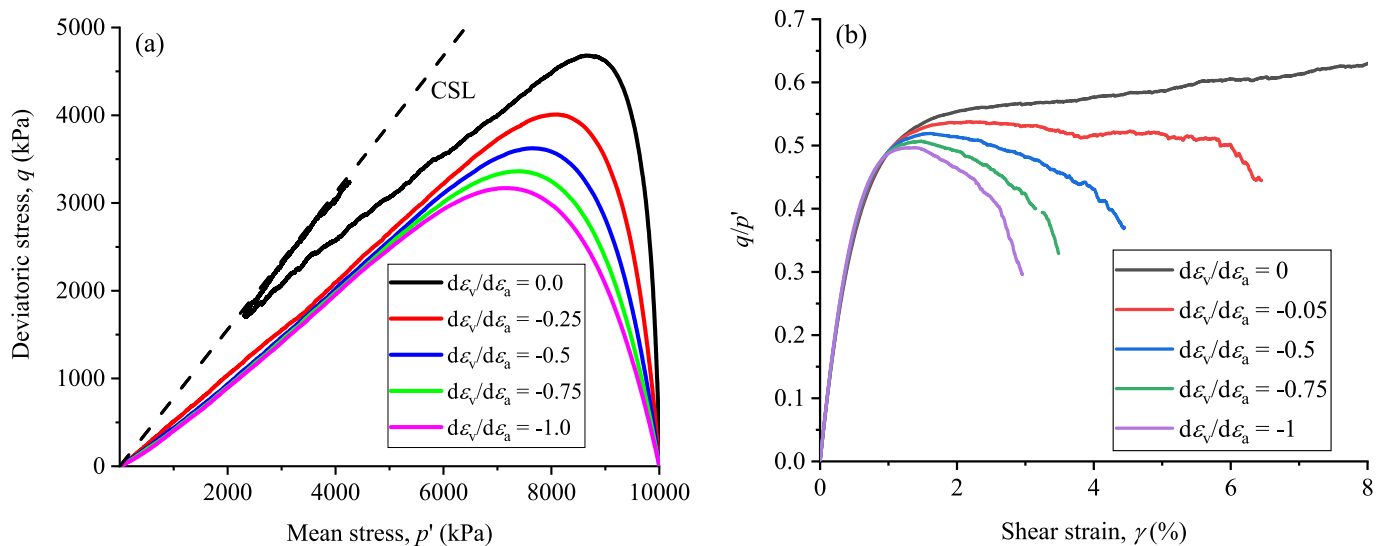

Fig. 8. DEM simulations of proportional stretching along dilative strain paths from an initial state with $p'_0 = 10$ MPa: a) stress path response and b) stress ratio – shear strain response.
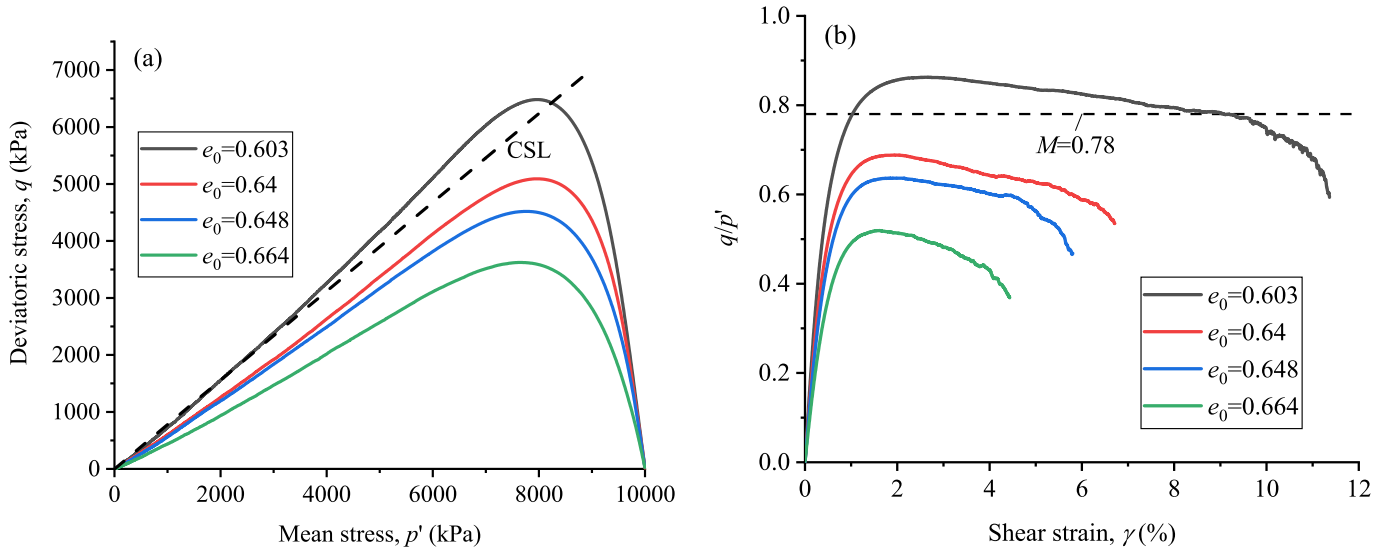
Fig. 9. Effect of sample initial density (e_0) on the proportional stretching response for $d\varepsilon_v/d\varepsilon_a$ = -0.5: a) stress path response and b) stress ratio – shear strain response.
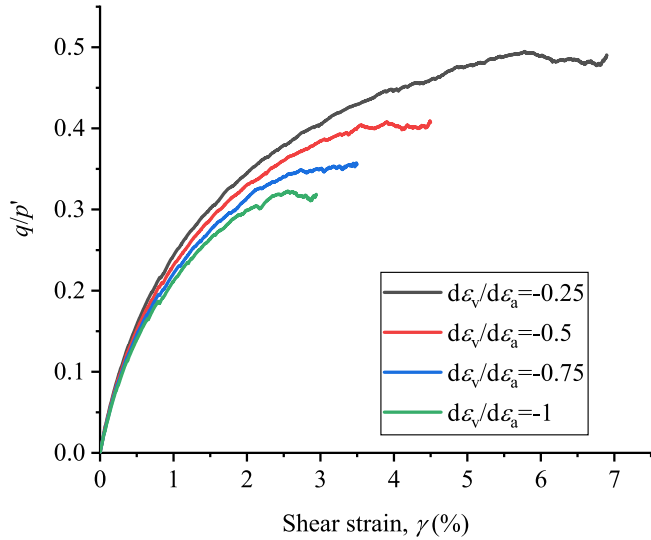

Fig. 10. Stress ratio response along contractive proportional strain paths simulated using rigid wall boundaries.

sample than that of an initially loaded sample.

In previous DEM studies on proportional shearing, 'pseudo' asymptotic states with constant stress ratios have been attained using rigid wall boundaries, as discussed earlier. These constant stress ratio states appear as special cases of Eq. (6) with $\alpha \equiv 1$, indicating that the unique relationship described by Eq. (6) can be ultimately attained regardless of the boundary condition employed. However, Deng et al. (2021) demonstrated that the reason for constant stress ratios to emerge in their DEM simulations along dilative proportional strain paths is due to the occurrence of a shear band whose response closely follows the critical state line. This suggests that 'pseudo' asymptotic states are manifestations of the same critical state in the presence of nonhomogeneous deformations. In contrast, the observations shown in Fig. 11 illustrate the response of samples with uniform deformations since periodic boundaries were used, thereby representing the true asymptotic behaviour.

4. Analysis of responses at the micro scale

The microscopic responses were analysed to explain why constant stress ratios were not achieved and to explore the microscopic characteristics of the granular material behaviour along proportional strain paths. Understanding the variation of material fabric along these paths offers insights into the changing mechanism governing material behaviour under varying shearing modes. The findings are also anticipated to inform the development of fabric evolution laws, as existing models (Gao and Zhao, 2013; Wang et al., 2020; Zhao and Kruyt, 2020) do not consider the anisotropy variations along general proportional paths.

In cohesionless granular materials, external stresses are transmitted through material packing via an inhomogeneous network of interparticle contacts. Radjai et al. (1998) revealed that this contact network has a prominent bimodal characteristic. The contacts bearing above-average contact forces (referred to as strong contacts) take the dominant role in transmitting the stress, while the contacts bearing under-average contact forces (referred to as weak contacts) serve to prop the subnetwork of strong contacts and dissipate kinetic energy. The microscopic response analysis has been conducted based on this characteristic.

4.1. Coordination number (CN)

CN is the average number of contacts per particle in a granular assembly and can be calculated as $CN = 2N_c/N_p$ where N_c and N_p are the number of contacts and particles in the assembly, respectively. For the quasi-static processes simulated in this study, CN simply reflects the geometric connectivity of the granular packing and may be taken as a measure of packing density (Jia et al., 2021; O'Sullivan, 2011). Compared to CN, the mechanical coordination number (MCN) proposed by Thornton (2000) provides a more representative measure of the connectivity in the load-bearing structures in the assembly because the particles and contacts isolated from the stress transmission network are excluded from the calculation of MCN given by Eq. (7).

$$\text{MCN} = \frac{2\left(N_c - N_p^1\right)}{N_p - N_p^0 - N_p^1} \tag{7}$$

where N_p^1 is the number of particles with only one contact and N_p^0 is the number of floating particles that do not contact others.

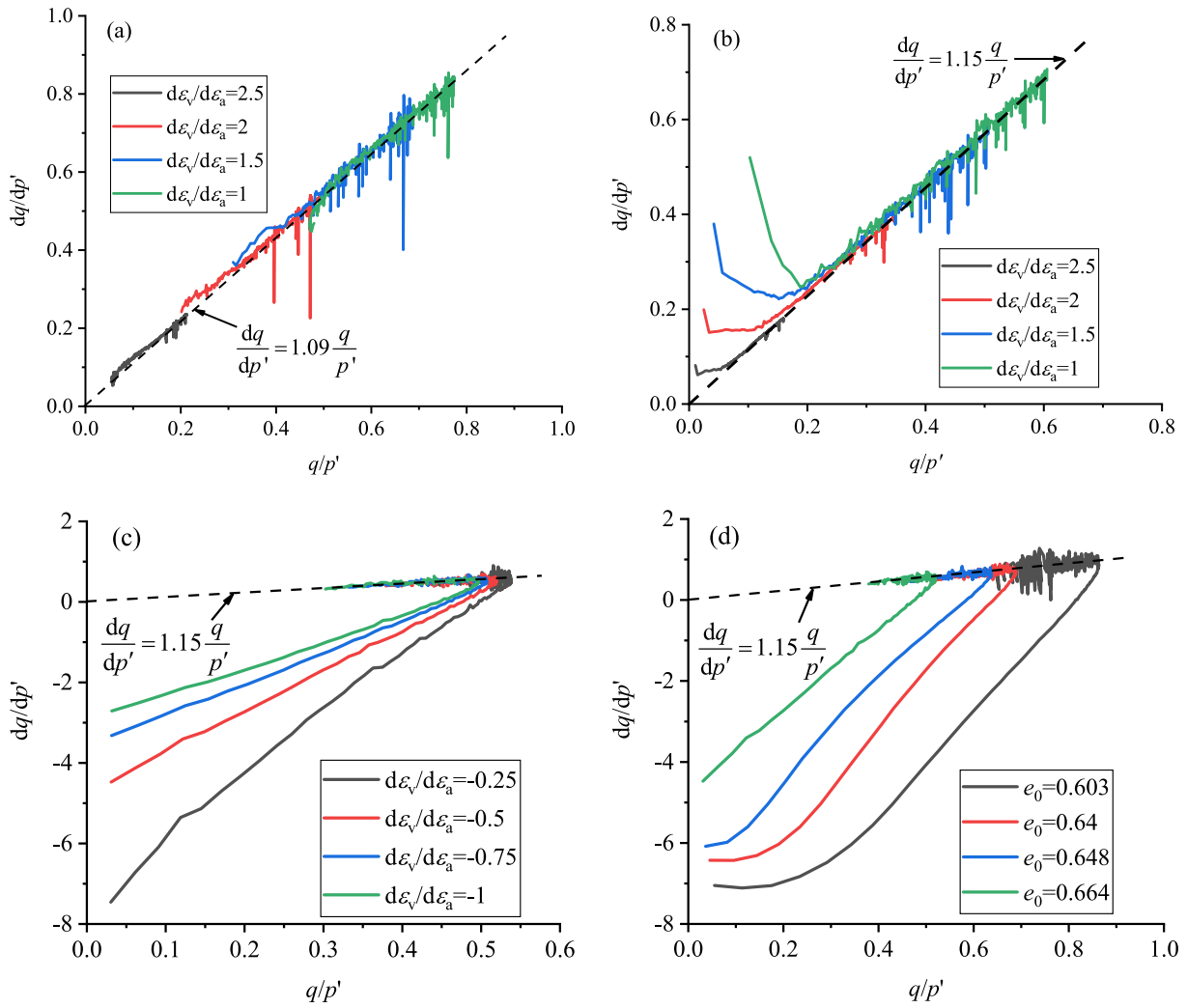Fig. 13 shows the variation of CN and MCN with p' along contractive

Fig. 11. Relationship between dq/dp' and q/p' for simulations along a) contractive strain paths initiated from the stress-free state, b) contractive strain paths initiated from $p'_0 = 10$ kPa, c) dilative strain paths initiated from $p'_0 = 10$ MPa, and d) $d\varepsilon_v/d\varepsilon_a = -0.5$ path on samples of different initial void ratio e_0.
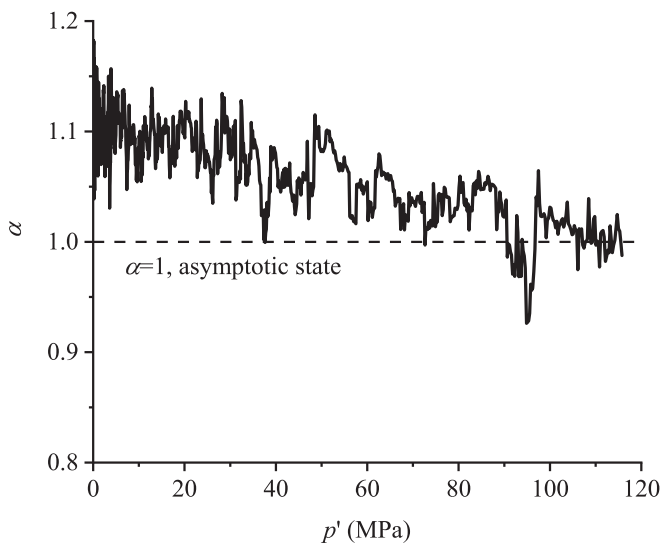

Fig. 12. Variation of α in the prolonged shearing simulation with $d\varepsilon_v/d\varepsilon_a = 0.5$ and $p'_0 = 10$ kPa

strain path simulations from Group B and dilative strain path

simulations from Group C. As expected, both CN and MCN increase with p' along contractive strain paths where the density increases ($d\varepsilon_v/d\varepsilon_a > 0$), and they decrease with the decrease of p' along dilative strain paths with $d\varepsilon_v/d\varepsilon_a < 0$. This demonstrates a positive correlation between packing density and CN/MCN across all strain path simulations. Fig. 13 (a) shows that when $d\varepsilon_v/d\varepsilon_a < 2$, both CN and MCN are higher for more contractive strain paths (greater $d\varepsilon_v/d\varepsilon_a$). However, for $d\varepsilon_v/d\varepsilon_a \geq 2$, the response of CN and MCN appears almost unaffected by $d\varepsilon_v/d\varepsilon_a$. A similar observation can be found in Fig. 14 where the responses of CN and MCN are plotted against the void ratio (e) in the assembly for the same two sets of simulations. Fig. 14, on the one hand, shows that there is no unique relationship between CN/MCN and e, indicating the effect of fabric anisotropy on CN/MCN, as it has been revealed in various studies (Kozicki et al., 2014; Rothenburg and Kruyt, 2004; Thornton, 2000). More importantly, it is observed from Fig. 14(a) that both the CN – e and MCN – e relationships converge to single lines for $d\varepsilon_v/d\varepsilon_a \geq 2$, just as the relationship with p' shown in Fig. 13(a). The insensitivity of MCN and CN to the change of strain path direction for $d\varepsilon_v/d\varepsilon_a \geq 2$ suggests that isotropic microstructural properties such as CN and MCN fail to char-acterise the stress response of granular materials sheared along highly contractive strain paths.

For the variation of CN and MCN along dilative strain paths shown in Fig. 13(b) and 14(b), it is observed that there is a better agreement between the CN/MCN – p' relationships for different values of $d\varepsilon_v/d\varepsilon_a$
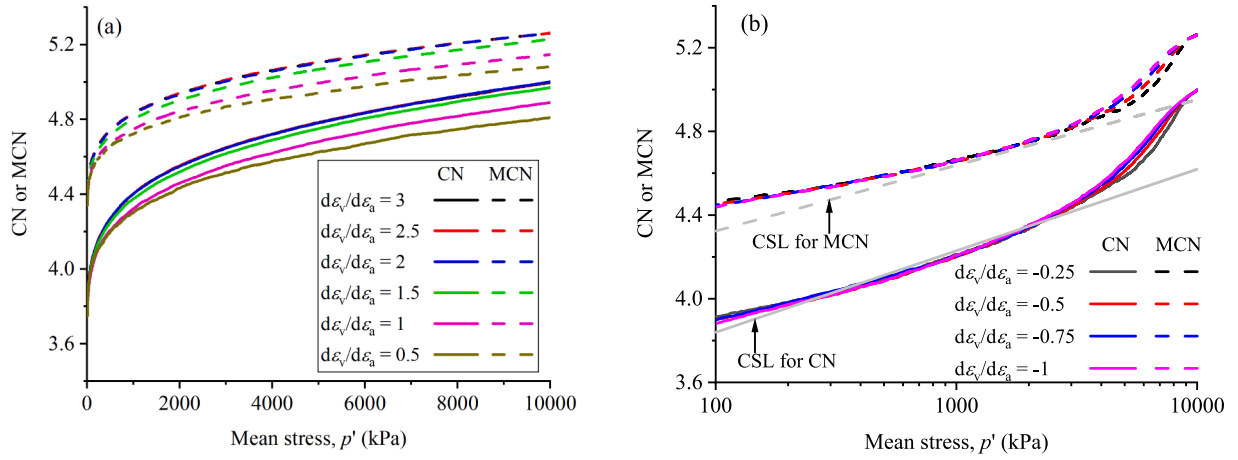
Fig. 13. Variation of coordination number (CN) and mechanical coordination number (MCN) with mean effective stress (p') in the simulations along a) contractive proportional strain paths initiated from $p'_0 = 10$kPa and b) dilative strain paths.
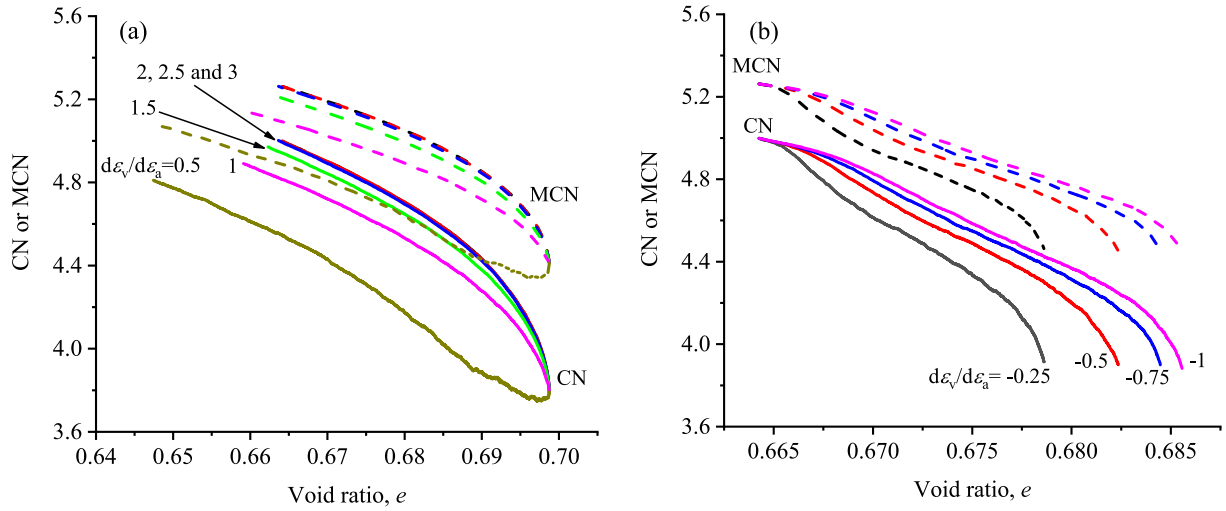

Fig. 14. Variation of coordination number (CN) and mechanical coordination number (MCN) with void ratio (e) in the simulations along a) contractive proportional strain paths initiated from $p'_0 = 10$kPa and b) dilative strain paths.

than between the CN/MCN – e relationships. Specifically, the CN/MCN – p' relationships for different $d\varepsilon_v/d\varepsilon_a$ almost converge to a single line after p' drops below 3000 kPa. Referring to Fig. 8(a), it is found that for $p' \leq 3000$ kPa, the stress paths for different $d\varepsilon_v/d\varepsilon_a$ almost overlapped. Additionally, when p' decreases below about 3000 kPa, the trajectory of CN in Fig. 13(b) closely follows the CSL for CN obtained from drained triaxial shear simulations with $\sigma'_3 = 50$, 100 and 200 kPa, while the MCN trajectory lies slightly above the corresponding CSL.

Comparing the findings from the contractive and dilative strain path simulations, it is found that CN and MCN exhibit a decreasing ability to characterise the stress response of a granular material as $d\varepsilon_v/d\varepsilon_a$ increases. As it will be shown later, this is because CN and MCN are geometric characteristics of the packing, and with the increase of $d\varepsilon_v/d\varepsilon_a$, the contribution of geometric characteristics to material behaviour gradually decreases while mechanical characteristics become increasingly more dominant.

4.2. Contact force distribution and contact partition

Complementary to the microstructural properties (CN and MCN) studied above, this subsection examines the micromechanical properties of the contact network in terms of contact force distribution and fraction of strong/weak contacts. According to the photoelastic experiments

performed by Majmudar and Behringer (2005), while the distribution of contact normal forces evolves for different loading paths imposed onto the sample, the general form of the contact tangential force distribution does not appear to be sensitive to the loading condition. Therefore, only the distribution of contact normal forces (f_n) will be examined.

Fig. 15 presents the distribution of contact normal forces at $p'=10$ MPa in samples loaded along different contractive proportional strain paths with $d\varepsilon_v/d\varepsilon_a$ ranging from 0.5 to 3 from $p'=10$ kPa (Group B). The normalised contact density shown in the figure was calculated as the number of contacts in each of 100 force groups, divided by the expected contact number in that group for a uniform distribution (i.e. $N_c/100$). The figure shows that with the decrease of $d\varepsilon_v/d\varepsilon_a$ in the contractive range, there is a trend for the peak of the normal force distribution to shift towards lower contact forces. This agrees with the observation by Antony (2001) that at high levels of strength mobilisation (low values of $d\varepsilon_v/d\varepsilon_a$; see Fig. 6(a)), the contact density exhibits an exponential decay with the increase of f_n throughout the entire distribution; close to the isotropic state (e.g. $d\varepsilon_v/d\varepsilon_a = 3$), the contact density decays exponentially for f_n greater than the average contact normal force $< f_n >$ and exhibits a half-Gaussian distribution for f_n smaller than $< f_n >$. The contact normal force distribution at $p'=100$ kPa along dilative strain paths, as shown in Fig. 15(b), clearly exhibits the trend typical of high mobilised strength and has no clear dependence on $d\varepsilon_v/d\varepsilon_a$. These
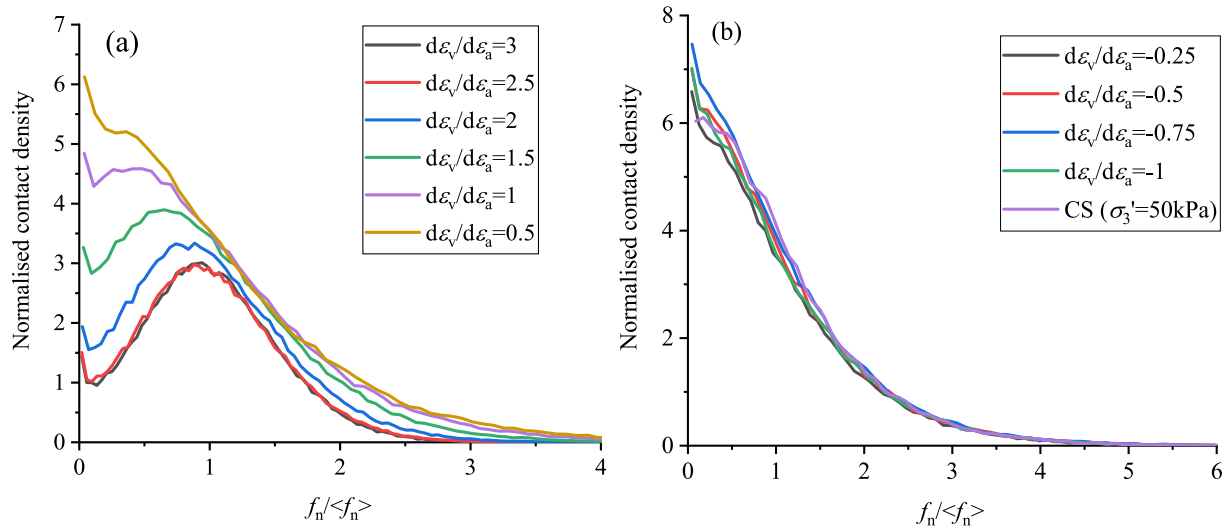
Fig. 15. Distribution of normalised contact density with normalised normal force $f_n/\langle f_n \rangle$ at a) $p'=10$ MPa in contractive strain path simulations initiated from $p'_0 = 10$ kPa and b) $p'=100$ kPa in dilative strain path simulations.

distributions resemble that at the CS in the conventional drained triaxial shear simulation with $\sigma'_3 = 50$ kPa, which is also presented in Fig. 15(b). Note that the contact normal force distribution at the CS remains almost unchanged for σ'_3 spanning from 50 to 500 kPa.

To quantitatively evaluate the contact normal force distributions, the $\langle f_n \rangle$, coefficient of variation (COV) and maximum ($f_{n,max}$) for different strain path simulations are calculated and presented in Fig. 16. The $\langle f_n \rangle$ and $f_{n,max}$ are normalised with respective to $p' \bullet d_{50}^2$ since they were obtained at different p' in dilative and contractive strain path simulations. The figure shows that the COV in the contact normal force distribution initially increases as $d\varepsilon_v/d\varepsilon_a$ decreases, stabilising around the COV observed at the CS from the drained simulations. This suggests that, as the strain path deviates from the isotropic case ($d\varepsilon_v/d\varepsilon_a = 3$), the contact normal force distribution becomes increasingly more nonuniform. In contrast, the normalised $\langle f_n \rangle$ remains almost unaffected by $d\varepsilon_v/d\varepsilon_a$, with the values obtained from dilative strain path simulations at $p' = 100$ kPa being slightly greater than those from the contractive strain path simulation at $p' = 10$ MPa. Additionally, the normalised $f_{n,max}$ increases with the decrease of $d\varepsilon_v/d\varepsilon_a$. Both the normalised $\langle f_n \rangle$ and $f_{n,}$

$_{max}$ do not show a tendency to approach a CS value, which contrasts with the response of the COV. This can be explained by the fact that the COV at CS is nearly independent of p', while the CS values of $\langle f_n \rangle$ and $f_{n,max}$ decrease with the increase of p' (not shown for simplicity). The latter response is attributed to the increase of CN with p'.

To relate the contact force distribution to the load-bearing capacity of the granular packing, the fractions of strong and weak contacts in the proportional strain path simulations are presented in Fig. 17. The DEM simulation results reported by Guo and Zhao (2013) suggested that the variation in strong and weak contact fractions appears relatively insensitive to the state of sample or modes of shearing, but associates closely with the strength mobilisation levels in the material. In their simulations, the fraction of weak contacts increases with increasing stress ratio. This can be interpreted as a need for more lateral support (weak contacts) to stabilise the strong force chains (strong contacts) at elevated strength mobilisation levels.

In Fig. 17, as the distribution of contact normal forces becomes more nonuniform (i.e. $d\varepsilon_v/d\varepsilon_a$ decreases), the fraction of strong contacts decreases and that of weak contacts increases. This observation aligns with the high COV values shown in Fig. 16, indicating that mobilising high strength in granular materials necessitates the formation of a non-homogeneous contact network where large contact forces are borne by a few strong contacts, while the majority of contacts provide support to stabilise these highly stressed force chains. Interestingly, Fig. 17 also shows that after an initial nonlinear behaviour, the fractions of strong and weak contacts in all these simulations reach a steady-state value. Besides, although not presented here, in the other simulations performed in this study (simulations in Group A and D, and conventional triaxial tests), the ratios of strong and weak contacts also reach steady-state values that are independent of the confining pressure or initial conditions. Overall, it can be concluded that proportional strain paths are characterised by a constant partition ratio between strong and weak contacts. The variation of these steady-state values of strong and weak contact fractions with $d\varepsilon_v/d\varepsilon_a$ is illustrated in Fig. 18 where the steady-state values for the simulations with $d\varepsilon_v/d\varepsilon_a > 0$ and $d\varepsilon_v/d\varepsilon_a < 0$ were taken at $p'=10$ MPa and 100 kPa, respectively. The CS values indicated in the figure were obtained from the drained triaxial simulations. From Fig. 18, it is observed that the steady-state fraction of strong contacts reduces as $d\varepsilon_v/d\varepsilon_a$ decreases until it stabilises at the CS value for $d\varepsilon_v/d\varepsilon_a \leq 0$. The strong contact fraction at CS appears to be a limiting value for all proportional strain paths.

Combining the observations from Fig. 13(b), Fig. 15(b) and Fig. 17 (b), it can be concluded that the micro-structure of the samples under
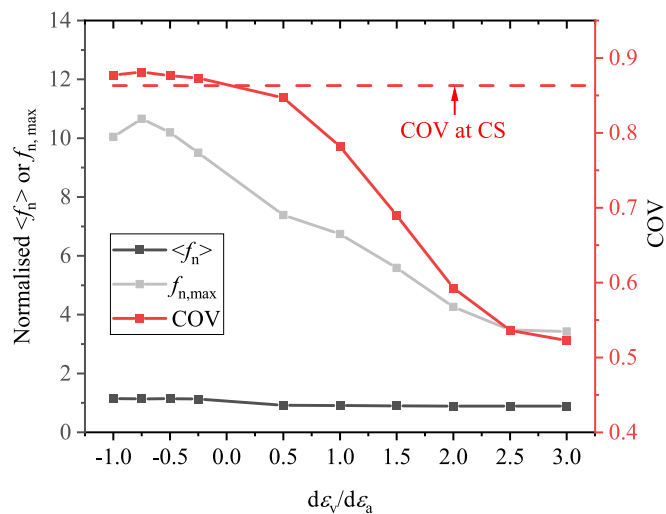

Fig. 16. Effect of $d\varepsilon_v/d\varepsilon_a$ on the normalised average and maximum contact normal force ($\langle f_n \rangle$ and $f_{n,max}$) and on the coefficient of variance (COV) of the contact normal forces.
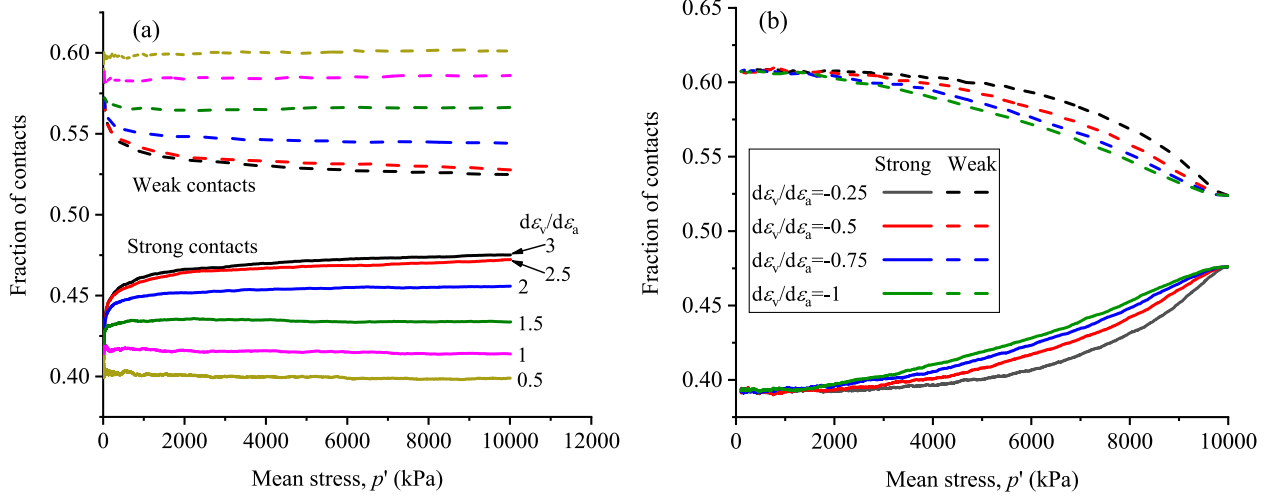
Fig. 17. Variation of the fraction of strong and weak contacts in the simulations along a) contractive strain paths initiated from $p'_0 = 10$ kPa and b) dilative strain paths.
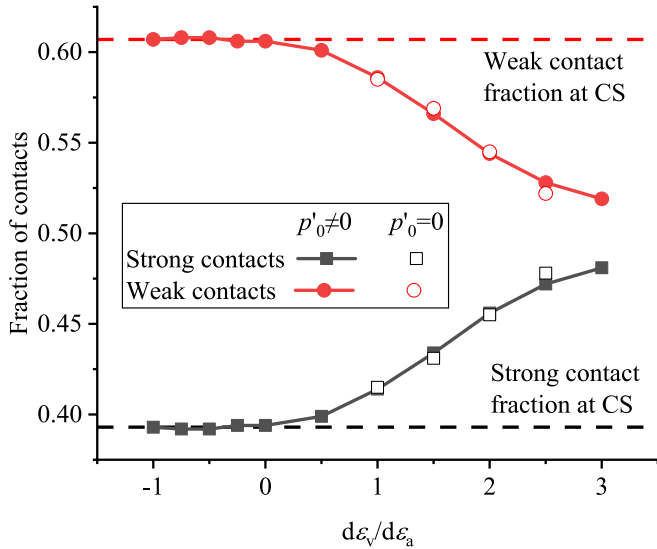

Fig. 18. Variation of steady-state values of strong and weak contact fractions with strain path directions.

various dilative strain paths is statistically similar to that at the CS in terms of CN, contact force distribution, and contact partition ratios. The reason for this similarity is that the CS is a limiting state where shearing can continue without increasing the stress or altering the packing volume. Therefore, the CS fabric reflects the minimal requirement to maintain the stability of a granular packing at a limiting state. Thus, the results shown in Fig. 13(b), Fig. 15(b) and Fig. 17(b) actually indicate that the granular packing also attains a limiting state when subjected to dilative strain path shearing. It is noted that CN, contact force distribution and contact partition ratios studied above are isotropic measures of material fabric. The orientational distribution of contact and contact forces will be studied in the next section.

4.3. Geometric and mechanical anisotropies

A key aspect of granular material behaviour is their ability to develop anisotropic fabric and contact force distribution that memorise the previous loading history and affect the subsequent response to external loading (Chaudhary et al., 2002; Gutierrez and Ishihara, 2000; Kruyt and Rothenburg, 2016; Liu et al., 2024, among others). The anisotropy

in relation to the spatial arrangement of particles and associated voids is referred to as geometric anisotropy, whereas that reflecting the anisotropic distribution of contact forces is called mechanical anisotropy (Cambou et al., 2004). There are different ways to measure the geometric and mechanical anisotropies (Guo and Zhao, 2013; Kanatani, 1984; Li and Li, 2009; Oda and Iwashita, 1999; Sitharam et al., 2009). In this study, the geometric anisotropy is characterised by the orientational distributions of contact normal vectors and branch vectors given by tensors a^c_{ij} and a^d_{ij}, which can be calculated from Eqs. (8) and (9), respectively (Ouadfel and Rothenburg, 2001).

$$a^c_{ij} = \frac{15}{2}\Phi'_{ij} \tag{8}$$

$$a^d_{ij} = \frac{15}{2}\frac{d'_{ij}}{\bar{d}^0} \tag{9}$$

where Φ'_{ij} is the deviatoric part of the contact orientation fabric tensor Φ_{ij} defined by Oda (1982) as:

$$\Phi_{ij} = \frac{1}{N_c}\sum_{c \in N_c} n_i n_j \tag{10}$$

where n_i and n_j are the i and j components of the unit contact normal vector; d'_{ij} is the deviatoric part of the branch vector fabric tensor d_{ij} given by Eq. (11) and $\bar{d}^0$ is the trace of d_{ij}.

$$d_{ij} = \frac{1}{N_c}\sum_{c \in N_c} \frac{d^c n_i n_j}{1 + a^c_{kl} n_k n_l} \tag{11}$$

where d^c is the length of the branch vector, and Einstein's summation convention applies.

The mechanical anisotropy is studied separately for the contact normal and tangential forces using the anisotropy tensors a^n_{ij} and a^t_{ij}, which can be calculated with Eqs. (12) and (13) respectively.

$$a^n_{ij} = \frac{15}{2}\frac{f'^n_{ij}}{\bar{f}^0} \tag{12}$$

$$a^t_{ij} = \frac{15}{3}\frac{f'^t_{ij}}{\bar{f}^0} \tag{13}$$

where f^n_{ij} and f^t_{ij} are the deviatoric parts of the contact normal and tangential force anisotropy tensors f^n_{ij} and f^t_{ij} given by Eqs. (14) and (15)

respectively, and $\bar{f}^0$ is the trace of f_{ij}^n.

$$f_{ij}^n = \frac{1}{N_c} \sum_{c \in N_c} \frac{f_n n_i n_j}{1 + a_{kl}^c n_k n_l} \tag{14}$$

$$f_{ij}^t = \frac{1}{N_c} \sum_{c \in N_c} \frac{f_s t_i n_j}{1 + a_{kl}^c n_k n_l} \tag{15}$$

where f_n and f_s are the contact normal and tangential forces, and t_i is the i component of the unit contact tangential vector.

The reason to select these four anisotropy tensors as indicators is that there exists a stress–force–fabric relationship that correlates the stress ratio in a granular assembly to the invariant of these tensors according to (Chantawarungal, 1993; Guo and Zhao, 2013; Rothenburg and Bathurst, 1989):

$$\frac{q}{p'} = \frac{2}{5} \left(a_c + a_d + a_n + \frac{3}{2} a_t \right) \tag{16}$$

where a_c, a_d, a_n and a_t are the signed deviatoric invariants of tensors a_{ij}^c, a_{ij}^d, a_{ij}^n and a_{ij}^t respectively, calculated using:

$$a_* = \text{sign}(J_*) \sqrt{\frac{3}{2} a_{ij}^* a_{ij}^*} \tag{17}$$

where a_* represents a_c, a_d, a_n or a_t when the sub/superscript * is c, d, n or t; J_* is the joint invariant of a_{ij}^* with the deviatoric stress tensor S_{ij} given by:

$$J_* = \frac{S_{ij} a_{ij}^*}{\sqrt{S_{ij} S_{ij}} \sqrt{a_{ij}^* a_{ij}^*}} \tag{18}$$

As explained by Rothenburg and Bathurst (1989), Equation (16) suggests that the ability of a non-cohesive granular material to bear deviatoric loads arises from its ability to develop an anisotropic contact network (reflected by a_c and a_d) and contact forces (reflected by a_n and a_t). In this sense, the four selected tensors provide a complete and complementary description of anisotropies relevant to the stress ratio response of the material.

Fig. 19 presents the variation of a_c, a_d, a_n and a_t along contractive ($d\varepsilon_v/d\varepsilon_a = 0.5$) and dilative ($d\varepsilon_v/d\varepsilon_a = -0.75$) proportional strain paths. For both simulations, the branch vector anisotropy a_d is found to be much smaller than the others, in agreement with existing studies where a_d is found to be negligible in narrowly graded packings of spherical particles (Guo and Zhao, 2013; Khakpour and Mirghasemi, 2023).
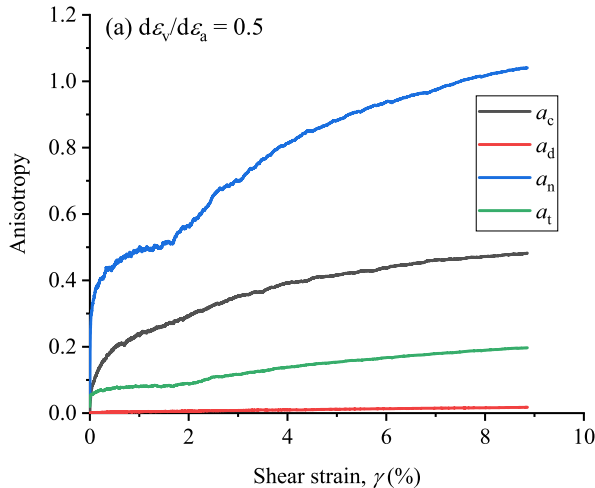
Furthermore, the results also suggest that Eq. (16) is applicable to proportional strain paths, as demonstrated in Fig. 20 where the stress ratio responses obtained with Eq. (16) are found to agree well with those directly recorded in the simulations. As already discussed earlier, the stress ratios in the two simulations with $d\varepsilon_v/d\varepsilon_a = 0.5$ and 0.75 do not attain constant values but instead continue to evolve with further shearing. This can be explained by the stress–force–fabric relationship and the fact that the anisotropies have not attained constant values, as seen in Fig. 19. Combining these results with the variation of CN and MCN presented in Fig. 13, it can be concluded that general proportional paths (except for $d\varepsilon_v/d\varepsilon_a = 3$ and 0) are associated with continuously evolving fabric isotropic factors (CN and MCN), fabric anisotropy (a_c and a_d) and mechanical anisotropy (a_n and a_t).

On the other hand, Eq. (16) allows the contribution from each anisotropy to the stress ratio within the material to be calculated, making it possible to evaluate the relative significance of mechanical and geometric anisotropies. Fig. 21 shows the contributing weight of the different anisotropies on the stress ratio, calculated according to Eq. (16). In the $d\varepsilon_v/d\varepsilon_a \geq 0$ cases, the contributing weight reached almost constant values, as illustrated in Fig. 21(a). This suggests that the rates of change in various anisotropies are synchronised to maintain a constant
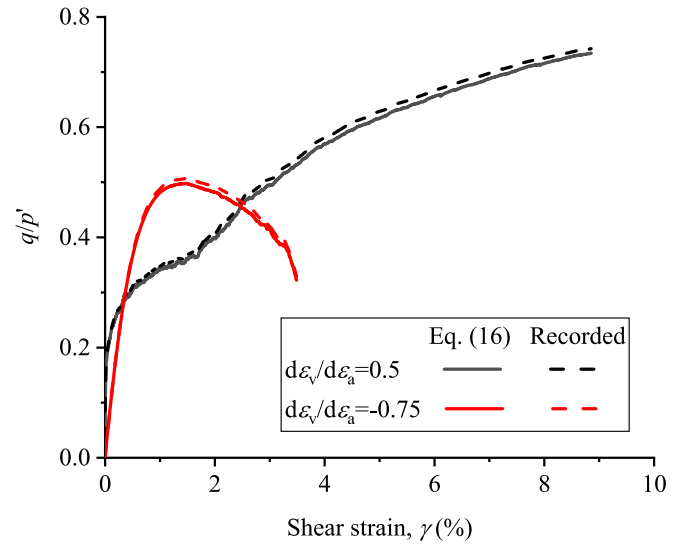

Fig. 20. Validation of the stress–force–fabric relationship for proportional strain paths.
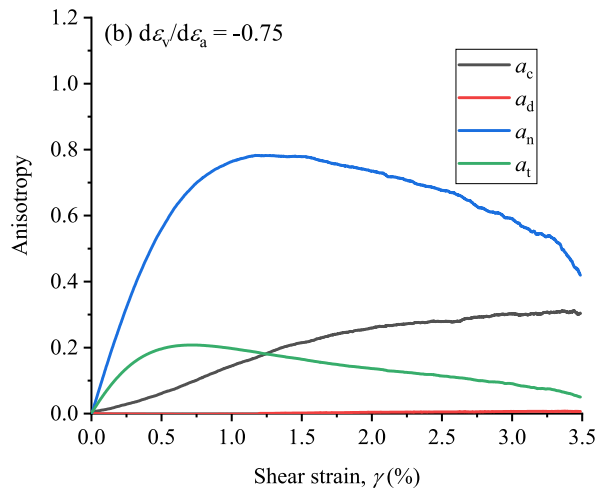

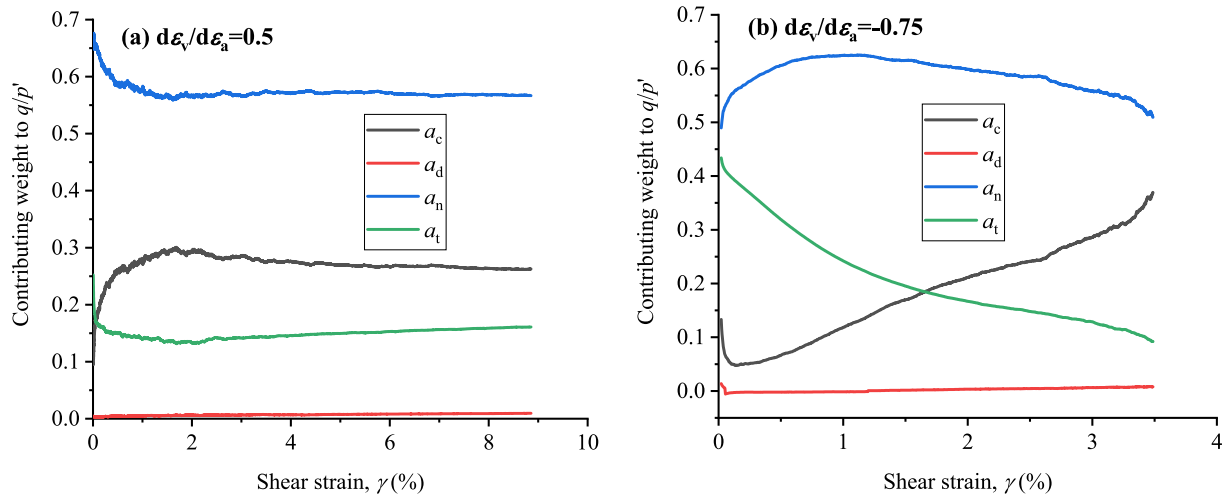**Fig. 19.** Typical responses of different anisotropies in proportional strain path simulations.

Fig. 21. Contributing weight of anisotropies of the distribution of contact orientation (a_c), branch vector (a_d), contact normal force (a_n) and contact shear force (a_t) in the mobilised shear strength of the sample, calculated according to Eq. (16).

ratio of their contributions to the mobilised shear strength of the material. As CN increases in contractive strain path simulations, this further indicates that the newly generated contacts contribute similarly to the geometric and mechanical anisotropies. However, when $d\varepsilon_v/d\varepsilon_a < 0$, such as the case shown in Fig. 21(b), the contributing weight of a_c increased as proportional stretching continued while the weight of a_n and a_t decreased. This suggests that as the stress state approaches zero, the geometric anisotropy becomes increasingly more important in the mobilised strength of the material. Despite this trend, it should be pointed out that in all simulations conducted in this study, the mechanical anisotropy (a_n and a_t) is found to be the major source of shear strength in the granular assembly, even for dilative strain path simulations at stress levels as low as $p' = 1$ kPa. This phenomenon is linked to the fact that spherical particles are used in the simulations.

To understand how strain path direction affects the relative importance of geometric and mechanical anisotropies to the load-bearing capacity of the granular packing, the steady-state contributing weights of various anisotropy terms in the stress ratio q/p' are plotted against $d\varepsilon_v/d\varepsilon_a$ in Fig. 22. The steady-state value was calculated as the average over the last 1 % shear strain in each simulation. The dilative strain path

simulations were excluded from this analysis as the weights did not exhibit a steady state, as shown earlier.

Fig. 22 shows that, as the strain path becomes less contractive (lower $d\varepsilon_v/d\varepsilon_a$), the steady-state contributing weight of the mechanical anisotropy (a_n and a_t) in the mobilised shear strength decreases while the weight of the geometric anisotropy (a_c and a_d) increases. Because a lower $d\varepsilon_v/d\varepsilon_a$ means a more deviatoric straining mode, the above observation can be alternatively understood as that the significance of the geometric anisotropy increases as the straining mode becomes more deviatoric. This is most effectively demonstrated by the asymptotic state associated with isotropic compression ($d\varepsilon_v/d\varepsilon_a = 3$) where the geometric characteristics of particles have no influence on the stress ratio response. In addition, the evolution of the geometric anisotropy with the strain path direction agrees with the decreasing ability of CN/MCN to characterise the mechanical behaviour of granular material as $d\varepsilon_v/d\varepsilon_a$ increases, as observed in Section 4.1.

5. Summary

This study has presented the results of DEM simulations to investigate the asymptotic behaviour of granular materials under proportional shearing along different strain path directions and from different initial stress/density conditions. The simulation conditions/parameters were carefully selected to ensure realistic and quasi-static modelling of a granular assembly consisting of spherical particles along a wide spectrum of proportional strain paths while suppressing shear band formation.

The simulation results suggest that for contractive strain paths, Goldscheider's two rules regarding the asymptotic behaviour are generally valid, although general asymptotic states may not be practically attainable. The effect of particle breakage on the asymptotic behaviour should be clarified in the future. On the other hand, the two rules appear invalid for dilative proportional strain paths because granular materials under such paths will ultimately liquefy and the stress ratio does not exhibit any tendency to stabilise. Despite this difference, a proportional $dq/dp' - q/p'$ relationship has been identified as a common characteristic for both dilative and contractive proportional strain paths, and the slope of this relationship appears insensitive to strain path direction and initial stress/density conditions.

At the particle scale, the asymptotic behaviour is characterised by a contact network with varying topological structures, indicated by changes in CN and MCN values, and a constant partition ratio between strong and weak contacts. The steady-state fraction of strong contacts decreases as the strain path becomes more dilative, eventually
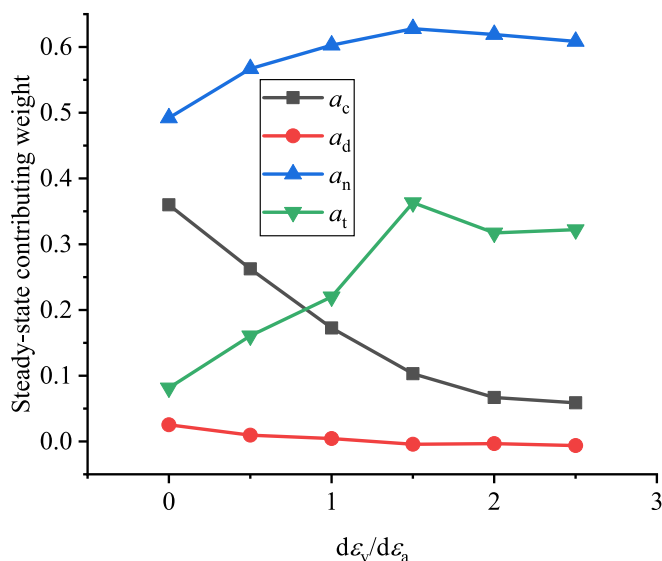

Fig. 22. Effect of strain path direction on the contributing weight of various anisotropy terms to q/p' at the steady state.

stabilising at the CS value for constant-volume and dilative strain paths. The micro-structure of samples under dilative strain paths is statistically similar to that at the CS in terms of CN, contact force distribution, and contact partition ratios since the CS fabric represents the minimal requirement to maintain the stability of the granular packing at a limiting state.

The capacity of a non-cohesive granular material to carry deviatoric stresses is due to its ability to develop non-uniform, anisotropic distributions of contacts and contact forces. The current simulations show that along proportional strain paths, except for the cases with $d\varepsilon_v/d\varepsilon_a = 0$ and 3, the geometric isotropy (CN and MCN) and anisotropy (a_c and a_d) and the mechanical anisotropy (a_n and a_t) all continue to evolve. However, for contractive proportional strain paths, the rates of change in different anisotropies are synchronised to maintain a constant ratio of their contributions to the mobilised shear strength of the material. The ratio of the contribution of geometric anisotropy increases as the strain path becomes more dilative. Nevertheless, the mechanical anisotropy remains the major source of mobilised shear strength in all the simulations for granular materials with spherical particles.

This study only considered a narrowly graded assembly of unbreakable spherical particles. Further investigations into the effect of particle strength, particle shape and size distribution on the asymptotic behaviour of granular materials could provide important insights into how particle-scale characteristics and their evolution can affect the attainability of an asymptotic state.

CRediT authorship contribution statement

Bo Liu: Writing – original draft, Visualization, Methodology, Investigation, Formal analysis, Conceptualization. **Zhen-Yu Yin:** Writing – review & editing, Project administration, Methodology, Funding acquisition, Conceptualization. **Pierre-Yves Hicher:** Writing – review & editing, Methodology.

Declaration of competing interest

The authors declare that they have no known competing financial interests or personal relationships that could have appeared to influence the work reported in this paper.

Acknowledgement

Data availability

Data will be made available on request.

References

Alonso-Marroquín, F., Luding, S., Herrmann, H.J., Vardoulakis, I., 2005. Role of anisotropy in the elastoplastic response of a polygonal packing. Phys. Rev. E Stat. Nonlin. Soft Matter Phys. 71, 1–18. https://doi.org/10.1103/PhysRevE.71.051304.

Antony, S.J., 2001. Evolution of force distribution in three-dimensional granular media. Phys. Rev. E Stat. Nonlin. Soft Matter Phys. 63, 011302. https://doi.org/10.1103/PhysRevE.63.011302.

Bauer, E., Kovtunenko, V.A., Krejčí, P., Krenn, N., Siváková, L., Zubkova, A.V., 2020. On proportional deformation paths in hypoplasticity. Acta Mech. 231, 1603–1619. https://doi.org/10.1007/s00707-019-02597-3.

Cambou, B., Dubujet, P., Nouguier-Lehon, C., 2004. Anisotropy in granular materials at different scales. Mechanics of Materials 36, 1185–1194. https://doi.org/10.1016/j.mechmat.2002.12.002.

Cavarretta, I., 2009. The influence of particle characteristics on the engineering behaviour of granular materials. University of London, Imperial College London.

Cerfontaine, B., Ciantia, M., Brown, M.J., Sharif, Y.U., 2021. DEM study of particle scale and penetration rate on the installation mechanisms of screw piles in sand. Comput. Geotech. 139, 104380. https://doi.org/10.1016/j.compgeo.2021.104380.

Chantawarungal, K., 1993. Numerical simulations of three dimensional granular assemblies. University of Waterloo, Ontario, Canada.

Chaudhary, S.K., Kuwano, J., Hashimoto, S., Hayano, Y., Nakamura, Y., 2002. Effect of initial fabric and shearing direction on cyclic deformation characteristics of sand. Soils Found. 42, 147–157.

Cho, G.-C., Dodds, J., Santamarina, J.C., 2006. Particle shape effects on packing density, stiffness, and strength: natural and crushed sands. J. Geotech. Geoenviron. 132, 591–602. https://doi.org/10.1061/(asce)1090-0241(2006)132:5(591).

Chu, J., Lo, S.-C.-R., 1994. Asymptotic behaviour of a granular soil in strain path testing. Géotechnique 44, 65–82. https://doi.org/10.1680/geot.1995.45.2.337.

Chu, J., Lo, S.C.R., Lee, I.K., 1996. Strain softening and shear band formation of sand in multi-axial testing. Géotechnique 46, 63–82. https://doi.org/10.1680/geot.1996.46.1.63.

Chu, J., Lo, S.C.R., Lee, I.K., 1993. Instability of granular soils under strain path testing. Journal of Geotechnical Engineering 119, 874–892. https://doi.org/10.1061/(ASCE)0733-9410(1993)119:5(874).

Cundall, P.A., 1988. Computer simulations of dense sphere assemblies. In: Satake, M., Jenkins, J.T.B.T.-S. (Eds.), Micromechanics of Granular Materials. Elsevier, Amsterdam, the Netherlands, pp. 113–123.

Da Cruz, F., Emam, S., Prochnow, M., Roux, J.N., Chevoir, F., 2005. Rheophysics of dense granular materials: Discrete simulation of plane shear flows. Phys Rev. E Stat. Nonlin. Soft Matter Phys. 72, 1–17. https://doi.org/10.1103/PhysRevE.72.021309.

Daouadji, A., Jrad, M., Robin, G., Brara, A., Daya, E.M., 2017. Phase transformation states of loose and dense granular materials under proportional strain loading. J. Eng. Mech. 143, 1–7. https://doi.org/10.1061/(asce)em.1943-7889.0001056.

Darve, F., Sibille, L., Daouadji, A., Nicot, F., 2007. Bifurcations in granular media: macro- and micro-mechanics approaches. Comptes Rendus - Mecanique 335, 496–515. https://doi.org/10.1016/j.crme.2007.08.005.

Deng, N., Wautier, A., Thiery, Y., Yin, Z.Y., Hicher, P.Y., Nicot, F., 2021. On the attraction power of critical state in granular materials. J. Mech. Phys. Solids 149, 104300. https://doi.org/10.1016/j.jmps.2021.104300.

Fei, W., Narsilio, G.A., 2020. Impact of three-dimensional sphericity and roundness on coordination number. J. Geotech. Geoenviron. 146, 1–7. https://doi.org/10.1061/(asce)gt.1943-5606.0002389.

Gao, Z., Zhao, J., 2013. Strain localization and fabric evolution in sand. Int. J. Solids Struct. 50, 3634–3648. https://doi.org/10.1016/j.ijsolstr.2013.07.005.

Goldscheider, M., 1976. Grenzbedingung und fliessregel von sand. Mech. Res. Commun. 3, 463–468. https://doi.org/10.1016/0093-6413(76)90037-9.

Grabco, D., Palistrant, M., Shikimaka, R., Zhitaru, R., Rahvalov, V., Zugravescu, D., 2002. Hardness and brittleness of rocks studied by microindentation method in combination with the registration of acoustic emission signals. 8th European Conference on Non-Destructive Testing.

Gudehus, G., Goldscheider, M., Winter, H., 1977. Mechanical properties of sand and clay and numerical integration methods: some sources of errors and bounds of accuracy. In: Gudehus, G. (Ed.), Finite Elements in Geomechanics. Wiley-Interscience, pp. 121–150.

Guo, N., Zhao, J., 2013. The signature of shear-induced anisotropy in granular media. Comput. Geotech. 47, 1–15.

Gutierrez, M., Ishihara, K., 2000. Non-coaxiality and energy dissipation in granular materials. Soils Found. 40, 49–59. https://doi.org/10.3208/sandf.40.2_49.

Hardin, B.O., 1985. Crushing of soil particles. J. Geotechnical Eng. 111, 1177–1192. https://doi.org/10.1061/(ASCE)0733-9410(1985)111:10(1177).

Hicher, P.Y., 1998. Experimental behaviour of granular materials. In: Cambou, B. (Ed.), Behaviour of Granular Materials. Springer, Wien, Austria, pp. 1–97.

Huang, X., Hanley, K.J., O'Sullivan, C., Kwok, C.Y., 2014. Exploring the influence of interparticle friction on critical state behaviour using DEM. Int. J. Numer. Anal. Methods Geomech. 38, 1276–1297. https://doi.org/10.1002/nag.2259.

Ibraim, E., Lanier, J., Wood, D.M., Viggiani, G., 2010. Strain path controlled shear tests on an analogue granular material. Géotechnique 60, 545–559. https://doi.org/10.1680/geot.8.P.100.

Jia, M., Liu, B., Xue, J., Ma, G., 2021. Coupled three-dimensional discrete element–finite difference simulation of dynamic compaction. Acta Geotech. https://doi.org/10.1007/s11440-020-01055-y.

Jop, P., Forterre, Y., Pouliquen, O., 2006. A constitutive law for dense granular flows. Nature 441, 727–730. https://doi.org/10.1038/nature04801.

Jrad, M., Sukumaran, B., Daouadji, A., 2012. Experimental analyses of the behaviour of saturated granular materials during axisymmetric proportional strain paths. Eur. J. Environ. Civ. En. 16, 111–120. https://doi.org/10.1080/19648189.2012.666900.

Kanatani, K., 1984. Distribution of directional data and fabric tensor. Int. J. Eng. Sci. 22, 149–164. https://doi.org/10.1016/0020-7225(84)90090-9.

Khakpour, M., Mirghasemi, A.A., 2023. Macro-micro mechanical study of principal stress rotation in granular materials using DEM simulations of hollow cylinder test. Powder Technol. 425, 118580. https://doi.org/10.1016/j.powtec.2023.118580.

Kolymbas, D., 2012. Barodesy: A new constitutive frame for soils. Géotechnique Letters 2, 17–23. https://doi.org/10.1680/geolett.12.00004.

Kozicki, J., Tejchman, J., Mühlhaus, H.-B., 2014. Discrete simulations of a triaxial compression test for sand by DEM. Int. J. Numer. Anal. Methods Geomech. 38, 1923–1952. https://doi.org/10.1002/nag.2285.

Kruyt, N.P., Rothenburg, L., 2016. A micromechanical study of dilatancy of granular materials. J. Mech. Phys. Solids 95, 411–427. https://doi.org/10.1016/j.jmps.2016.01.019.

Kumar, R., Gopireddy, S.R., Jana, A.K., Patel, C.M., 2020. Study of the discharge behavior of Rosin-Rammler particle-size distributions from hopper by discrete element method: A systematic analysis of mass flow rate, segregation and velocity profiles. Powder Technol. 360, 818–834. https://doi.org/10.1016/j.powtec.2019.09.044.

Lade, P.V., Yamamuro, J.A., Bopp, P.A., 1996. Significance of particle crushing in granular materials. Journal of Geotechnical Engineering 122, 309–316. https://doi.org/10.1061/(ASCE)0733-9410(1996)122:4(309).

Lancelot, L., Shahrour, I., Al Mahmoud, M., 2004. Instability and static liquefaction on proportional strain paths for sand at low stresses. J. Eng. Mech. 130, 1365–1372. https://doi.org/10.1061/(asce)0733-9399(2004)130:11(1365).

Lensky, V.S., 1960. Analysis of plastic behaviour of metals under complex loading. In: Lee, E.H., Symonds, P.S. (Eds.), Proceedings of the Second Symposium on Naval Structural Mechanics. Pergamon Press, Providence, Rhode Island, US, pp. 259–278.

Li, X., Li, X.S., 2009. Micro-macro quantification of the internal structure of granular materials. J. Eng. Mech. 135, 641–656. https://doi.org/10.1061/(asce)0733-9399(2009)135:7(641).

Liu, B., Liu, Z., Jin, J., Yin, Z.Y., 2024. Micromechanical investigation of the effect of an imposed stress state change during drained cyclic loading using DEM. Comput. Geotech. 166, 105998. https://doi.org/10.1016/j.compgeo.2023.105998.

Luo, T., Yao, Y., Chu, J., 2009. Asymptotic state behaviour and its modeling for saturated sand. Sci. China Ser. E 52, 2350–2358.

Majmudar, T.S., Behringer, R.P., 2005. Contact force measurements and stress-induced anisotropy in granular materials. Nature 435, 1079–1082. https://doi.org/10.1038/nature03805.

Mašín, D., 2013. Clay hypoplasticity with explicitly defined asymptotic states. Acta Geotech. 8, 481–496.

Mašín, D., 2012. Asymptotic behaviour of granular materials. Granul. Matter 14, 759–774. https://doi.org/10.1007/s10035-012-0372-x.

Mašín, D., Jerman, J., 2015. Discrete element investigation of rate effects on the asymptotic behaviour of granular materials. In: Rinaldi, V.A., Zeballos, M.E., Clariá, J.J. (Eds.), 6th International Symposium on Deformation Characteristics of Geomaterials. IOS Press, Buenos Aires, Argentina, pp. 695–702. https://doi.org/10.3233/978-1-61499-601-9-695.

Medicus, G., Kolymbas, D., Fellin, W., 2016. Proportional stress and strain paths in barodesy. Int. J. Numer. Anal. Methods Geomech. 40, 509–522.

Mindlin, R.D., Deresiewicz, H., 1953. Elastic spheres in contact under varying oblique forces. J. Appl. Mech. 20, 327–344.

Nguyen, H.B.K., Rahman, M.M., Fourie, A.B., 2018. Characteristic behavior of drained and undrained triaxial compression tests: DEM study. J. Geotech. Geoenviron. 144, 4018060. https://doi.org/10.1061/(ASCE)GT.1943-5606.0001940.

Nicot, F., Daouadji, A., Hadda, N., Jrad, M., Darve, F., 2013. Granular media failure along triaxial proportional strain paths. Eur. J. Environ. Civ. En. 17, 777–790. https://doi.org/10.1080/19648189.2013.819301.

Oda, M., 1982. Fabric tensor for discontinuous geological materials. Soils Found. 22, 96–108. https://doi.org/10.3208/sandf1972.22.4_96.

Oda, M., Iwashita, K., 1999. Mechanics of granular materials: An introduction. Balkema, Netherlands, A.A.

O'Sullivan, C., 2011. Particulate discrete element modelling: a geomechanics perspective. CRC Press.

Ouadfel, H., Rothenburg, L., 2001. 'Stress-force-fabric' relationship for assemblies of ellipsoids. Mechanics of Materials 33, 201–221. https://doi.org/10.1016/S0167-6636(00)00057-0.

Perfect, E., Xu, Q., Terry, D.L., 1998. Improved Parameterization of Fertilizer Particle Size Distribution. J. AOAC Int. 81, 935–942. https://doi.org/10.1093/jaoac/81.5.935.

Radjai, F., Wolf, D., Jean, M., Moreau, J.J., 1998. Bimodal character of stress transmission in granular packings. Phys. Rev. Lett. 80, 61–64.

Rothenburg, L., Bathurst, R.J., 1989. Analytical study of induced anisotropy in idealized granular materials. Géotechnique 39, 601–614. https://doi.org/10.1680/geot.1989.39.4.601.

Rothenburg, L., Kruyt, N.P., 2004. Critical state and evolution of coordination number in simulated granular materials. Int. J. Solids Struct. 41, 5763–5774. https://doi.org/10.1016/j.ijsolstr.2004.06.001.

Santamarina, J.C., Cho, G.C., 2004. Soil behaviour: The role of particle shape. In: Advances in Geotechnical Engineering: the Skempton Conference - Proceedings of a Three Day Conference on Advances in Geotechnical Engineering. Institution of Civil Engineers, pp. 604–617.

Shi, J., Guo, P., 2017. Modelling fabric evolution of granular materials along proportional strain paths. In: Papamichos, E., Papanastasiou, P., Pasternak, E., Dyskin, A. (Eds.), Proceedings of the 11th International Workshop on Bifurcation and Degradation in Geomaterials Dedicated to Hans Muhlhaus, pp. 373–379.

Sibille, L., Hadda, N., Nicot, F., Tordesillas, A., Darve, F., 2015. Granular plasticity, a contribution from discrete mechanics. J. Mech. Phys. Solids 75, 119–139. https://doi.org/10.1016/j.jmps.2014.09.010.

Sitharam, T.G., Vinod, J.S., Ravishankar, B.V., 2009. Post-liquefaction undrained monotonie behaviour of sands: Experiments and DEM simulations. Géotechnique 59, 739–749. https://doi.org/10.1680/geot.7.00040.

Thornton, C., 2000. Numerical simulations of deviatoric shear deformation of granular media. Géotechnique 50, 43–53.

Thornton, C., Antony, S.J., 2000. Quasi-static shear deformation of a soft particle system. Powder Technol. 109, 179–191.

Topolnicki, M., Gudehus, G., Mazurkiewicz, B.K., 1990. Observed stress-strain behaviour of remoulded saturated clay under plane strain conditions. Géotechnique 40, 155–187. https://doi.org/10.1680/geot.1990.40.2.155.

Wanatowski, D., 2007. Asymptotic behaviour of sand in plane-strain compression tests. Studia Geotechnica et Mechanica XXIX, 19–44.

Wanatowski, D., Chu, J., Lo, R.S.C., 2008. Strain-softening behaviour of sand in strain path testing under plane-strain conditions. Acta Geotech. 3, 99–114. https://doi.org/10.1007/s11440-008-0064-1.

Wang, R., Dafalias, Y.F., Fu, P., Zhang, J.M., 2020. Fabric evolution and dilatancy within anisotropic critical state theory guided and validated by DEM. Int. J. Solids Struct. 188–189, 210–222. https://doi.org/10.1016/j.ijsolstr.2019.10.013.

Wu, Q., Faraji, S.F., Zheng, Y., Zheng, J.J., 2024. Effects of intermediate principal stress on the granular material behavior under partial drainage conditions. Acta Geotech. 19, 2629–2648. https://doi.org/10.1007/s11440-024-02292-1.

Zhao, C.F., Kruyt, N.P., 2020. An evolution law for fabric anisotropy and its application in micromechanical modelling of granular materials. Int. J. Solids Struct. 196–197, 53–66. https://doi.org/10.1016/j.ijsolstr.2020.04.007.

Zhou, W., Liu, J., Ma, G., Yuan, W., Chang, X., 2016. Macroscopic and microscopic behaviors of granular materials under proportional strain path: a DEM study. Int. J. Numer. Anal. Methods Geomech. 40, 2450–2467.